

## Continental-scale contributions to the global CFC-11 emission increase between 2012 and 2017

Lei Hu<sup>1,2</sup>, Stephen A. Montzka<sup>2</sup>, Fred Moore<sup>1,2</sup>, Eric Hintsa<sup>1,2</sup>, Geoff Dutton<sup>1,2</sup>, M. Carolina Siso<sup>1,2</sup>, Kirk Thoning<sup>2</sup>, Robert W. Portmann<sup>3</sup>, Kathryn McKain<sup>1,2</sup>, Colm Sweeney<sup>2</sup>, Isaac Vimont<sup>1,2</sup>, David Nance<sup>1,2</sup>, Bradley Hall<sup>2</sup>, Steven Wofsy<sup>4</sup>

<sup>1</sup> Cooperative Institute for Research in Environmental Sciences, University of Colorado-Boulder, Boulder, CO, USA

<sup>2</sup> Global Monitoring Laboratory, NOAA, Boulder, CO, USA

<sup>3</sup> Chemical Science Laboratory, NOAA, Boulder, CO, USA

<sup>4</sup> Department of Earth and Planetary Sciences, Harvard University, Boston, MA, USA

Correspondence to: Lei Hu ([lei.hu@noaa.gov](mailto:lei.hu@noaa.gov))

**Abstract.** The detection of increasing global CFC-11 emissions after 2012, alerted society to a possible violation of the Montreal Protocol on Substances that Deplete the Ozone Layer (MP). This alert resulted in parties to the MP taking urgent actions. As a result, atmospheric measurements made in 2019 suggest a sharp decline in global CFC-11 emissions. Despite the success in the detection and mitigation of part of this problem, regions fully responsible for the recent global emission changes of CFC-11 have not yet been identified. Roughly two thirds ( $60 \pm 40\%$ ) of the emission increase between 2008 - 2012 and 2014 - 2017 and two thirds ( $60 \pm 30\%$ ) of the decline between 2014 - 2017 and 2019 were explained by regional emission changes in eastern mainland China. Here, we used atmospheric CFC-11 measurements made from two global aircraft surveys, the HIAPER Pole-to-Pole Observations (HIPPO) in November 2009 – September 2011 and the Atmospheric Tomography Mission (ATom) in August 2016 – May 2018, in combination with the global CFC-11 measurements made by the US National Oceanic and Atmospheric Administration during these two periods, to derive global and regional emission changes of CFC-11. Our results suggest Asia accounted for the largest fractions of global CFC-11 emissions in both periods, 43 (37 – 52) % during November 2009 – September 2011 and 57 (49 – 62) % during August 2016 – May 2018. Asia was also primarily responsible for the emission increase between these two periods, accounting for 86 (59 – 115) % of the global CFC-11 emission rise between the two periods. Besides eastern mainland China, temperate western Asia and tropical Asia also contributed significantly to global CFC-11 emissions during both periods and likely to the global CFC-11 emission increase. The atmospheric observations further provide strong constraints on CFC-11 emissions from North America and Europe, suggesting that each of them accounted for 10 – 15 % of global CFC-11 emissions during the HIPPO period and smaller fractions in the ATom period. For South America, Africa, and Australia, the derived regional emissions had larger dependence on the prior assumptions of emissions and emission changes, due to a lower sensitivity of the observations considered here to emissions from these regions. However, significant increases in CFC-11 emissions from southern hemispheric lands were not likely due to the observed increase of north-to-south interhemispheric gradients in atmospheric CFC-11 mole fractions from 2012 to 2017.

Deleted: Wofsy<sup>5</sup>

Deleted: NOAA,

Deleted: NOAA,

Deleted: <sup>4</sup> University of Maryland, MD, USA<sup>5</sup>

Formatted: Font color: Black

Deleted: lei.hu@noaa.gov

Formatted: Font color: Black

Deleted: An early

Deleted: a

Deleted: emission increase of

Deleted: (Montzka et al., 2018)

Deleted: early

Deleted: participating in

Deleted: (United Nations Environment Programme (UNEP), 2019).

Deleted: (Montzka et al., 2021).

Deleted: early

Deleted: some

Deleted: emission

Deleted: was

Deleted: (Park et al., 2021; Rigby et al., 2019).

Deleted: i.e.,

Deleted: Observation

Deleted: U.S.

Deleted: we find that

Deleted: between these periods. Besides Asia, the

Deleted: also

Deleted: the

Deleted: –

74 **1. Introduction**

75 Trichlorofluoromethane, CFC-11, is a potent ozone depleting substance, whose production  
76 has been controlled by the Montreal Protocol since 1987. By 2010, reported global production  
77 and consumption of CFC-11 was near zero (United Nations Environment Programme (UNEP),  
78 2021a, b). Corresponding to the declining production and consumption, global emissions of CFC-  
79 11 declined between 1988 and 2012. By 2012, the global CFC-11 emission magnitude was 50 –  
80 80 Gg yr<sup>-1</sup> with this range being associated primarily with its uncertain atmospheric lifetime (Engel  
81 et al., 2018). The remaining emissions of CFC-11 were primarily from existing equipment and  
82 insulation foams, known as “CFC-11 banks”. However, a large increase of global CFC-11  
83 emission from 2012 – 2017 was discovered (Montzka et al., 2018; Rigby et al., 2019; Montzka et  
84 al., 2021), suggesting illicit CFC-11 production despite the global ban on production and  
85 consumption under the MP beginning in 2010. This surprisingly large increase of CFC-11  
86 emissions attracted great attention from scientists, policy makers, and industrial experts around the  
87 world (Montzka et al., 2018; Rigby et al., 2019; Dhomse et al., 2019; Ray et al., 2020; Adcock et  
88 al., 2020; Keeble et al., 2020; Chen et al., 2020), who sought information to enable rapid mitigation  
89 of the unexpectedly enhanced CFC-11 emissions and ensure no significant delay in the recovery  
90 of stratospheric ozone. Despite the international effort to understand the origin of this large global  
91 emission increase of CFC-11, only a portion of the emission rise (60 ± 40 %) could be explained  
92 by emission increases from eastern mainland China (Rigby et al., 2019; Adcock et al., 2020; Park  
93 et al., 2021). It remains unclear where the rest of the global CFC-11 emission increase originated.

94 Following the initial studies and announcements of anomalous CFC-11 emission increases,  
95 a surprisingly sharp decline in global CFC-11 emissions occurred from 2018 to 2019 (Montzka et  
96 al., 2021). This decline immediately followed the global emission rise and had a similar magnitude  
97 as the emission rise between 2012 and 2017, resulting in global CFC-11 emissions in 2019 being  
98 similar to the mean 2008 – 2012 value (Montzka et al., 2021). Interestingly, roughly the same  
99 proportion of this emission decrease (60 ± 30 %) can be explained by an emission drop in eastern  
100 mainland China (Park et al., 2021) during this period, similar to the contribution of eastern  
101 mainland China to the global CFC-11 emission rise earlier (60 ± 40 %).

102 In this study, we analyzed global CFC-11 measurements made from the HIAPER Pole-to-  
103 Pole Observations (HIPPO) in November 2009 – September 2011, the Atmospheric Tomography  
104 Mission (ATom) in August 2016 – May 2018 (Wofsy, 2018; Bourgeois et al., 2020) and concurrent  
105 CFC-11 measurements from the US National Oceanic and Atmospheric Administration (NOAA)  
106 global atmospheric sampling network (Montzka et al., 2018) and combined them with Lagrangian-  
107 based inverse modeling techniques (Hu et al., 2017) to quantify continental- and regional- scale  
108 CFC-11 emission estimates between both periods. Coincidentally, the timing of the HIPPO and  
109 ATom campaigns covered the periods when the global CFC-11 emissions were at the minimum  
110 and maximum before the CFC-11 emission decline in 2018 – 2019. Hereafter, we will refer  
111 November 2009 – September 2011 as the HIPPO period and August 2016 – May 2018 as the  
112 ATom period. Here we further investigate regional contributions to the global CFC-11 emission  
113 rise between these two periods.

114 **2. Methods**

115 **2.1. Overview**

116 To infer regional CFC-11 emissions from observed atmospheric mole fractions, we used a  
117 Bayesian inverse modeling framework following the method described in previous studies (Hu et  
118 al., 2015; Hu et al., 2017; Hu et al., 2016). In brief, the inverse modeling method assumes a linear  
119

Deleted: the

Deleted: emission dropping

Deleted: as

Deleted:

Deleted: Observation

Formatted: Font color: Black

Deleted: NOAA's

Deleted: our

relationship between measured atmospheric mole fraction enhancements and emissions upwind of the measurement locations. The linear operator, termed footprint, is the sensitivity of atmospheric mole fraction enhancements to upwind emissions, and it was computed for each sample using the Hybrid Single Particle Lagrangian Integrated Trajectory (HYSPPLIT) model described in Stein et al. (2015). Bayesian inverse models (Rodgers, 2000) require initial assumptions about the magnitudes and distributions of emissions, or prior emissions. By assuming that errors between the “true” and prior emissions and errors between atmospheric mole fraction observations and simulated mole fractions (using the computed footprints) follow Gaussian distributions, we construct a cost function ( $L$ ) (Eq. 1) based on Bayes’ Theorem:

$$L = \frac{1}{2}(z - Hs)^T R^{-1}(z - Hs) + \frac{1}{2}(s - s_p)^T Q^{-1}(s - s_p) \quad (1)$$

where,  $z$  represents the observed atmospheric enhancement relative to the upwind background atmosphere, (Section 2.2.3).  $s_p$  and  $s$  represent the prior and posterior CFC-11 emissions.  $H$  represents the Jacobian matrix or the first-order partial derivatives of  $z$  to  $s$ .  $R$  and  $Q$  stand for the model-data mismatch covariance and prior flux error covariance. The values given to  $R$  and  $Q$  determine the relative weight between the prior emission assumptions and atmospheric observations in the final solution. Here, we used the maximum likelihood estimation method (Hu et al., 2015; Michalak et al., 2005) and atmospheric observations to directly solve for site-dependent model-data mismatch errors and prior flux errors. For the aircraft campaigns (HIPPO and ATom), we derive separate model-data mismatch errors, one for each campaign.

## 2.2. Inversions for the HIPPO and ATom time intervals

In this section, we describe the detailed observation selection, estimating background mole fractions that were pre-subtracted from atmospheric observations before inversions, and prior emission assumptions for the global inversion we conducted for the HIPPO period (November 2009 – September 2011) and the ATom period (August 2016 – May 2018) using a Lagrangian inverse modeling approach.

### 2.2.1. CFC-11 measurements and data selection for global inversion analyses

All the CFC-11 measurements considered in our global inversion were made by the Global Monitoring Laboratory, NOAA, through four different sampling and measurement programs: the global aircraft surveys (flask samples collected during HIPPO and ATom), a global weekly surface flask sampling program, a global in situ sampling program, and a biweekly to monthly aircraft profiling sampling program primarily in North America (Fig. 1). CFC-11 measurements for the ATom campaigns were primarily made by a gas chromatography and mass spectrometry (GCMS) instrument (named “M3”) that was also dedicated for flask-air measurements in the global weekly surface flask program. Flask-air samples collected from the biweekly to monthly aircraft profiling sampling program and from the HIPPO campaign were analyzed by another dedicated GCMS instrument called “M2” and later upgraded to “PR1” in Sep 2014. Hourly in situ CFC-11 measurements were made by in situ gas chromatography with electron capture detector instruments (GC-ECDs) located at individual observatories (the Chromatograph for Atmospheric Trace Species, CATS). All the NOAA CFC-11 measurements were referenced to the same calibration scale (NOAA-2016) and suite of primary gravimetric standards. However, small differences were observed between results from the analysis of the same flask-air samples, on two different instruments (i.e., median differences: 0.7% between M3 and M2 during the HIPPO period and 0.9% between M3 and PR1 during ATom period; Fig. S1), and between results from samples

Deleted: upwind

Deleted: .

Deleted: footprints or

Deleted: sensitivities

Deleted: changes

Deleted: emission regions that were

Deleted: by time-inverted

Deleted: particle models

Deleted: ) and Nehr Korn et al. (2010). Because the inverse problem we generally solve is not fully constrained by the available number of atmospheric observations, the solution in a

Formatted: Font color: Auto

Deleted: inversion

Deleted: requires

Deleted: the

Deleted: .

Deleted: periods

Deleted: fraction estimation

Deleted: was

Deleted: -

Deleted: focused

Deleted: in measurements made

Deleted: that were analyzed by

Deleted: ) or measurements made for

196 collected within  $\pm 2$  hours that were analyzed by M3 (from flasks) and CATS (from in situ  
 197 instrumentation) (median differences were  $< 0.2\%$  during the HIPPO and ATom periods at three  
 198 relevant sites; Fig. S1). To minimize the influence of these artificial differences on derived fluxes,  
 199 particularly because the atmospheric CFC-11 signals associated with changing emissions were  
 200 extremely small (Montzka et al., 2021; Montzka et al., 2018), results from M2 and PR1 were scaled  
 201 to those from M3. Scaling factors were calculated over 3-month intervals for M2 and PR1 to make  
 202 them consistent for the same air-sample analyses. For the CATS measurements, fewer comparison  
 203 points were available, so scale adjustments of CATS data to M3 were based on one scaling factor  
 204 per site for the HIPPO period and, separately, the ATom period.

205 For measurements made during the HIPPO and ATom campaigns, we only include  
 206 measurements below 8 km in the global inversions to minimize the influence of stratospheric loss  
 207 on measured mole fractions and because high altitude samples typically have less emission  
 208 information. Some samples obtained below 8 km still retained a notable stratospheric loss signal,  
 209 and these data were also removed from further considerations on the basis of reduced mole  
 210 fractions observed for  $N_2O$ , which is useful for tracing stratospheric influence in an air parcel  
 211 owing to its small atmospheric variability and high-precision measurements.

212 For data obtained in NOAA's regular flask-air sampling programs, the inversions included  
 213 results from sites that are relatively far from recent anthropogenic emissions (i.e. sites many miles  
 214 away from populated areas or that are not situated in the boundary layer), in order to capture  
 215 emissions from broad regions. These observations include the weekly surface flask sampling at  
 216 remote, globally-distributed locations (Fig. 1) and aircraft profiling in Cook Islands and Alaska,  
 217 US, and above 1 km (above ground) over the contiguous US (Fig. 1). Most of our aircraft profiling  
 218 sampling was below 8 km above sea level.

219 To reduce the extremely large computing cost of footprint calculations for surface in situ  
 220 sampling, we chose a subset of in situ samples for inversion analyses. We randomly selected one  
 221 sample per day from sites such as Barrow, Alaska, US (BRW) and Tutuila, American Samoa  
 222 (SMO), and one daytime sample and one nighttime sample each day at Mauna Loa Observatory,  
 223 Hawaii, US (MLO). In situ measurements made at Summit, Greenland (SUM) were excluded due  
 224 to poorer precision of CFC-11 measurements made at this station.

225 Although many of the observations we used were from remote Pacific and Atlantic Oceans  
 226 locations, or from the free troposphere over North America, they did contain above-zero sensitivity  
 227 to emissive signals transported from all the continents, as shown in their footprints (Fig. 1); but  
 228 the overall sensitivity to emissions from South America, southern Africa, and Australia is low  
 229 relative to North American, Europe, and Asia (Fig. 1). Thus, observational constraints on  
 230 emissions from North America, Europe, and Asia are stronger and are less dependent on prior  
 231 assumptions compared to those from South America, Africa, and Australia.

### 2.2.2. Footprint simulations

232 We used the HYSPLIT model driven by the global data assimilation system at a  $0.5^\circ$   
 233 resolution (GDAS0.5 $^\circ$ ), to simulate footprints for our global inversion analyses. To determine an  
 234 adequate number of particles needed for this global simulation, we tested running HYSPLIT  
 235 backward for 45 days using 5000 and 10000 particles for a subset of observations obtained from  
 236 the second campaign during ATom (ATom-2). We compared the footprints from these two  
 237 independent simulations, which are only different by  $< 0.05\%$  in the total summed sensitivities.  
 238 Footprint distributions and magnitudes in individual time steps are also almost identical,  
 239 suggesting using 5000 particles was adequate for our global simulation.  
 240

Deleted: flask-air measurements

Deleted: measurements, i.e.,

Deleted: (

Deleted: , considered separately and derived from the collocated measurements collected within  $\pm 2$  hours

Deleted: our

Formatted: Font color: Auto

Deleted: away

Deleted: ,

Deleted: poor

Deleted: have reduced dependence

Deleted: American

Deleted: Hybrid Single-Particle Lagrangian Integrated Trajectory (

Deleted: )

Deleted: II



256 To determine an adequate time duration for each HYSPLIT simulation, we compared  
 257 footprints for observations with enhanced CFC-11 mole fractions versus those with relatively low  
 258 mole fractions for observations made at different altitudes and latitudes from ATom-2. Our results  
 259 show that, for observations in all [altitude](#) and [latitude](#) bins, those with enhanced CFC-11 mole  
 260 fractions always had higher sensitivity to upwind populated regions in the first 20 days (Fig. S2);  
 261 after that, the overall sensitivity was relatively small and constant, likely due to evenly distributed  
 262 particles throughout the troposphere beyond 20 days. This result suggests running HYSPLIT for  
 263 more than 20 days was likely sufficient for capturing the major emission influence on atmospheric  
 264 CFC-11 mole fraction observations made over the remote atmosphere. In the analysis presented  
 265 here, sensitivities were derived with HYSPLIT-GDAS0.5° by tracking 5000 particles back in time  
 266 for 30 days.

268 **2.2.3. Estimation of background mole fractions**

269 [As described above, emissions](#) are derived from measured mole fraction enhancements  
 270 above background values. For each observation, the background mole fraction was estimated  
 271 based on the 5000 HYSPLIT-GDAS0.5° back-trajectories and a [4D background mole fraction](#)  
 272 [field](#). We tested various approaches for constructing this 4D CFC-11 mole fraction field (see  
 273 [supplementary information; Figs. S3 and S4](#)). Here, we only describe the final choice selected for  
 274 [the inversion analysis](#). The final empirical 4D CFC-11 mole fraction field was constructed based  
 275 [on NOAA observations](#) by propagating a subset of measured mole fractions of CFC-11 from the  
 276 NOAA’s global surface and ongoing airborne flask-air sampling programs back in time along the  
 277 5000 back-trajectories for [10 days](#). Observations were [included in the background estimate if the](#)  
 278 [associated mole fraction was lower than the 70 – 80<sup>th</sup> percentile of all results](#) in each 30° in latitude  
 279 x 3 km in altitude box during the HIPPO period and [the 40 – 50<sup>th</sup> percentile of all results in each](#)  
 280 [box](#) during the ATom period. [These thresholds were chosen to ensure](#) that the inversely derived  
 281 global emissions in both periods were consistent with those derived from [a global 3 box model](#)  
 282 [and a best estimate of atmospheric CFC-11 lifetime](#) (Montzka et al., 2021). Although the inversely  
 283 derived global emission [total was](#) sensitive to the choice of the background threshold, the relative  
 284 regional emission distribution or the fraction of regional emissions to the global emission was  
 285 not. By propagating this subset of observations back in time, it provided a 4D field of CFC-11  
 286 [background](#) mole fractions that we then averaged every 5° latitude × 20° longitude × 2 km  
 287 [altitude](#) every month. [This 4D empirical background did not account for the strong](#) stratospheric  
 288 [influence](#) on CFC-11 mole fractions [at high altitudes](#) (8 - 10 km) in the polar regions (> 60°N or >  
 289 60°S). [Thus, we further scaled the CFC-11 mole fractions in these areas using](#) the vertical gradients  
 290 simulated by [the Whole Atmosphere Community Climate Model \(WACCM\) \(Davis et al., 2020;](#)  
 291 [Marsh et al., 2013; Montzka et al., 2021; Ray et al., 2020\)](#).

292 From [this 4D](#) background mole fraction field, we sampled 5000 mole fraction estimates at  
 293 the locations of the 5000 back-trajectories at the end of the 30 days and then averaged these 5000  
 294 mole fraction estimates to obtain one background mole fraction for each observation. We  
 295 examined the particle locations at the end of the 30 days using observations collected at 0 - 8 km  
 296 from ATom-2. For the majority of these observations, 80 % - 100 % of particles were located  
 297 between 0 and 10 km at the end of the 30 days in the HYSPLIT back-trajectory runs. For particles  
 298 that exited from the top at 10 km before 30 days, we sampled the mole fractions at 10 km when  
 299 they exited the background mole fraction field.

301 **2.2.4. Prior emissions**

- Deleted: II
- Deleted: altitudes
- Deleted: latitudes
- Deleted: Emissions
- Deleted: from the Lagrangian analysis
- Moved (insertion) [1]
- Deleted: background mole fraction field. We derived several background mole fraction fields for comparison. Initially, we examined the modeled 4D monthly CFC-11 mole fractions from the Whole Atmosphere Community Climate Model (WACCM) (Davis et al.,
- Moved down [2]: 2020; Marsh et al., 2013; Montzka et al., 2021; Ray et al., 2020).
- Deleted: In the WACCM simulation, global mole fractions [1]
- Deleted: a certain time duration. This subset of observations [2]
- Formatted: Font color: Auto
- Deleted: lower than a certain threshold
- Deleted: . We tested a range of thresholds between the 40<sup>th</sup> [3]
- Deleted: ones lower than
- Deleted: as background observations
- Deleted: , so
- Formatted: Font color: Auto
- Deleted: the
- Deleted: with different choices
- Formatted: Font color: Auto
- Deleted: lifetimes
- Deleted: magnitudes were
- Deleted: longitude
- Deleted: half or one
- Deleted: We tested the time duration of 10 – 30 days for. [4]
- Deleted: . We found propagating particles back in time for [5]
- Moved up [1]: S3 and S4).
- Deleted: We further added the influence of
- Deleted: air
- Deleted: high altitude
- Deleted: ) to this empirical background, by considering
- Moved (insertion) [2]
- Deleted: over these regions. As a result, this approach ... [6]
- Formatted: Font color: Auto
- Deleted: the
- Deleted: measurement-based
- Deleted: II

We constructed 11 different prior emission fields for inversion analyses in both the HIPPO and ATom periods (Fig. 2). The first prior emission field or “a priori” was constructed with an assumed global CFC-11 emission of 67 Gg yr<sup>-1</sup>. This global total was distributed around the globe in a 1° x 1° resolution based on a 1° x 1° gridded population density product from the Gridded Population of the World (GPW) v4 dataset (<https://sedac.ciesin.columbia.edu/data/collection/gpw-v4>). The only exception is over the US, where we used the 1° x 1° gridded annual emissions derived from Hu et al. (2017) for 2014. The second a priori emission has the same distribution as the first a priori, except the total emission magnitude was reduced by 40% across the globe, such that the global CFC-11 emission in this scenario is 40 Gg yr<sup>-1</sup>. The other 9 prior emission fields were constructed as the first a priori, but with an additional 20 Gg yr<sup>-1</sup> of emission imposed over North America, South America, Africa, Europe, Australia, boreal Asia, temperate eastern Asia, temperate western Asia, and tropical Asia. The 20 Gg yr<sup>-1</sup> of emissions was added to those regions by a constant emission rate in pmol m<sup>-2</sup> s<sup>-1</sup> across the grid cells, having non-zero emissions in the first prior emissions. The regions specified as North America (NA), South America (SA), Africa (AF), Europe (Eu), Australia (Au), boreal Asia (BA), temperate eastern Asia (TEA), temperate western Asia (TWA), and tropical Asia (TA) are shown in Fig. 3. We named the 11 different prior emission fields as “population GlobalEmission” or “population GlobalEmission region” (Fig. 2), where “population” represents their distribution; “GlobalEmission” represents the global emission in Gg yr<sup>-1</sup> in each prior; “region” represents the location where the additional 20 Gg yr<sup>-1</sup> of emission was added. For example, “population 87 TEA” indicates a priori with a global CFC-11 emission of 87 Gg yr<sup>-1</sup> and a distribution similar to population density; compared to the first a priori, this a priori had additional 20 Gg yr<sup>-1</sup> emissions imposed over TEA.

We assume an exponential decaying covariance function in the errors of prior emissions (Hu et al., 2017).

$$Q = \sigma_q^2 \begin{bmatrix} 1 & \exp\left(-\frac{h_{s,1,2}}{\tau_s}\right)\exp\left(-\frac{h_{t,1,2}}{\tau_t}\right) & \dots & \exp\left(-\frac{h_{s,1,m}}{\tau_s}\right)\exp\left(-\frac{h_{t,1,m}}{\tau_t}\right) \\ \exp\left(-\frac{h_{s,2,1}}{\tau_s}\right)\exp\left(-\frac{h_{t,2,1}}{\tau_t}\right) & 1 & \dots & \exp\left(-\frac{h_{s,2,m}}{\tau_s}\right)\exp\left(-\frac{h_{t,2,m}}{\tau_t}\right) \\ \vdots & \vdots & \ddots & \vdots \\ \exp\left(-\frac{h_{s,m,1}}{\tau_s}\right)\exp\left(-\frac{h_{t,m,1}}{\tau_t}\right) & \exp\left(-\frac{h_{s,m,2}}{\tau_s}\right)\exp\left(-\frac{h_{t,m,2}}{\tau_t}\right) & \dots & 1 \end{bmatrix} \quad (2)$$

where  $\sigma_q$  represents the 1 sigma error on a relative scale in the prior emission;  $\tau_t$  and  $\tau_s$  denote the spatial and temporal correlation lengths of prior emission error (the 95% correlation scales are approximately  $3\tau_t$  and  $3\tau_s$ ).  $h_t$  and  $h_s$  are temporal intervals and spatial distance between state vectors; and  $m$  stands for the number of state vectors.  $h_t$  and  $h_s$  can be calculated based on air sampling times and locations.  $\sigma_q$ ,  $\tau_s$ , and  $\tau_t$  are prior emission-dependent and were estimated by the maximum likelihood estimation.  $\sigma_q$  was estimated in a range of 200 – 340 % given the 9 different prior emission fields. The spatial and temporal correlation lengths were estimated as 2.5 km and 58 days. Prior uncertainty in regional emissions were then calculated by considering spatial and temporal correlations in space and time. The calculated 1- $\sigma$  uncertainty for the 9 different priors is 20 – 60% on a global scale and 20 – 120 % on a regional scale.

- Deleted: emissions
- Formatted: Space After: 0 pt
- Deleted: , “population\_67”,
- Deleted: a
- Deleted: and the posterior emissions derived for the contiguous US (CONUS) from Hu et al. (2017). Over the CONUS, the posterior annual 1° x 1° emissions derived for 2014 were applied to all months in either HIPPO or ATom periods. We then subtracted the annual total CONUS emissions (~ 4 Gg yr<sup>-1</sup>) from the
- Deleted: emission of 67 Gg yr<sup>-1</sup> and
- Deleted: the remaining emissions
- Deleted: prior, “population\_40”, was the
- Deleted: in “population\_67” with
- Deleted: magnitudes
- Deleted: . The priors “population\_87\_NA”, “population\_87\_SA”, “population\_87\_AF”, “population\_87\_Eu”, “population\_87\_Au”, “population\_87\_BA”, “population\_87\_TEA”, “population\_87\_TWA”, and “population\_87\_TA” incorporated the “population\_67” prior and
- Deleted: , respectively.
- Deleted: all
- Deleted: where emissions were
- Formatted: Font color: Black
- Deleted: of “population\_67”.
- Deleted: ,
- Deleted: ,
- Deleted: ,
- Deleted: ,
- Deleted: ,
- Deleted: ,
- Deleted: ,
- Deleted: ,
- Deleted: ,
- Deleted: ,

456 **2.2.5. Inversion ensembles**

457 We constructed 23 inversion ensembles for deriving global and regional emissions in the  
 458 HIPPO and ATom periods. These 23 inversion ensembles included 20 different prior emission  
 459 change scenarios between the HIPPO and ATom periods, two background CFC-11 mole fraction  
 460 fields, and two sets of observations (“flask only” and “flask + in situ”) (Table S1). The 20 prior  
 461 emission change scenarios assumed: (scenario 1) no increase of global CFC-11 emissions between  
 462 the HIPPO and ATom periods (inversion ensemble IDs #1 - #5 in Table S1); (scenario 2) a 20 Gg  
 463 yr<sup>-1</sup> increase of CFC-11 emissions between the HIPPO and ATom periods, with the increase being  
 464 restricted to one of the following regions, respectively: North America, South America, Africa,  
 465 Europe, Australia, boreal Asia, temperate eastern Asia, temperate western Asia, and tropical Asia  
 466 (inversion ensemble IDs #6 - #14 in Table S1); and (scenario 3) a 20 Gg yr<sup>-1</sup> decrease of CFC-11  
 467 emissions between the HIPPO and ATom periods, with the decrease being restricted to one of the  
 468 following regions, respectively: North America, South America, Africa, Europe, Australia, boreal  
 469 Asia, temperate eastern Asia, temperate western Asia, and tropical Asia (inversion ensemble IDs  
 470 #15 - #23 in Table S1).  
 471

472 In our global inversions, we solved for monthly 1° x 1° emissions and their posterior  
 473 covariances at 1° x 1° resolution. Because the uncertainty associated with the 1° x 1° emissions is  
 474 large, we aggregated emissions and their posterior covariances into regional, continental, and  
 475 global scales for the HIPPO and ATom periods, considering the cross correlation in errors among  
 476 grid cells and across times for each inversion (Hu et al., 2017). In this study, we report the mean  
 477 ( $\mu_i$ ) and 2 standard deviations ( $2\sigma_i$ ) of posterior estimates for each inversion scenario, where  $i$   
 478 denotes the inversion ID in Table S1. In the final results summarized in Table 1, we report two  
 479 types of uncertainties. The first uncertainty is calculated as the 2.5<sup>th</sup> – 97.5<sup>th</sup> percentile range of  
 480 the mean emissions ( $\mu_i$ ) derived from the 23 inversions, and are considered our “best estimates”  
 481 of emissions. Uncertainties were also calculated considering the uncertainty ( $2\sigma_i$ ) associated with  
 482 each inversion. The lower bound of this second uncertainty was calculated as the 2.5<sup>th</sup> percentile  
 483 of [ $\mu_1 - 2\sigma_1, \mu_2 - 2\sigma_2, \dots, \mu_{23} - 2\sigma_{23}$ ] and the upper bound was calculated as the 97.5<sup>th</sup> percentile  
 484 of [ $\mu_1 + 2\sigma_1, \mu_2 + 2\sigma_2, \dots, \mu_{23} + 2\sigma_{23}$ ].  
 485

486 **3. Results and Discussion**

487 **3.1. Increase of CFC-11 emissions between the HIPPO and ATom periods observed in remote**  
 488 **atmospheric observations**

489 The global increase of CFC-11 emissions between 2012 and 2017 was previously derived  
 490 from the slow-down in the decline of atmospheric CFC-11 mole fractions observed at Earth’s  
 491 surface (Montzka et al., 2021; Montzka et al., 2018) and is also shown in Fig. 4 here. Besides at  
 492 Earth’s surface, a similar magnitude of this slow-down in atmospheric CFC-11 mole fraction  
 493 decline is also apparent throughout the free troposphere in the aircraft profiles obtained during the  
 494 HIPPO and ATom campaigns, each of which involved sampling deployments spread over  
 495 approximately two years (Fig. 4). Here, we calculated the CFC-11 growth rates averaged in each  
 496 30° in latitude x 2 km in altitude box during HIPPO campaigns and during ATom campaigns  
 497 separately for samples collected above the Pacific Ocean basin. During HIPPO, we calculated the  
 498 average mole fraction differences in each 30° in latitude x 2 km in altitude box between HIPPO-  
 499 3 (3/2010 – 4/2010) and HIPPO-4 (6/2011 – 7/2011) and normalized by their time interval to  
 500 obtain annual growth rates, whereas we calculated annual growth rates during ATom using the

Deleted: large

Deleted: batch

Formatted: Indent: First line: 0"

Deleted: (Fig.

Deleted: 3

Deleted: III

Deleted: IV

ATom-1 (7/2016 – 8/2016) and ATom-4 (4/2018 – 5/2018) data. The reason to choose HIPPO-3, HIPPO-4, ATom-1, and ATom-4 for this calculation is to ensure annual growth rates were calculated from data collected in similar seasons, so that the impact of seasonal variations in atmospheric CFC-11 mole fractions on the calculated annual growth rates was minimized (Fig. S5). Results suggest a median growth rate of -2.5 ppt yr<sup>-1</sup> between 60°S and 90°N in the troposphere during the HIPPO period and a median growth rate of -0.7 ppt yr<sup>-1</sup> during the ATom period (Fig. 4), indicating a significant increase of CFC-11 growth rates in the troposphere between the HIPPO and ATom periods. The impact of the atmospheric CFC-11 seasonal cycle measured at the surface on the calculated changes of annual growth rates between both periods is about ±0.1 ppt. Besides the seasonal cycle of atmospheric CFC-11 mole fractions, the Quasi-Biennial Oscillation (QBO) can also influence atmospheric trace gas mole fractions in the troposphere (Ray et al., 2020) and thus their growth rates. However, this influence was smaller than the increase of the annual growth rates between the HIPPO and ATom periods, as quantified in Montzka et al. (2021).

After subtracting background CFC-11 mole fractions from the selected global CFC-11 observations, enhancements approaching 3 ppt were found in air above the Pacific Ocean basin during both sampling periods by all measurements methods (onboard the HIPPO and ATom aircraft surveys, from the global weekly flask sampling, and from the selected daily to “every other day” in situ sampling) (Fig. 5). Relatively larger enhancements were more frequently measured during the ATom period than during the HIPPO period (Fig. 5). However, the average increase in enhancements of the atmospheric CFC-11 mole fractions measured during ATom were 0.2 – 0.3 ppt higher than observed during the HIPPO campaign (Fig. 5). The 0.2 – 0.3 ppt increase in the atmospheric CFC-11 enhancements was also independently measured by the global weekly flask sampling, and in situ sampling networks over the Pacific Ocean basin (Fig. 5). Results from HIPPO and ATom suggest that increased mole fraction enhancements over the Pacific Ocean basin existed primarily between 0 and 60 °N (Fig. 5), where the lower and middle tropospheric air mainly contains emissive signals from Eurasia, western North America, and tropical America (Fig. S6). Furthermore, during ATom, CFC-11 enhancements measured in the Pacific Ocean basin were larger than those measured in the Atlantic Ocean basin (Fig. 5), suggesting regions immediately upwind of the Pacific Ocean were emitting more CFC-11 than regions upwind of the Atlantic Ocean (Fig. 1b) during the ATom period.

### 3.2. Regional emissions derived from HIPPO and ATom global inversions

#### 3.2.1. The base scenarios with only flask-air measurements

To quantitatively understand what measured atmospheric CFC-11 variability implies for global and regional CFC-11 emissions, we conducted Bayesian inversions as described in Section 2. We first only used the flask-air measurements made by the two GCMS instruments. These measurements include samples collected during HIPPO and ATom, the global weekly flask-air sampling program, and the regular aircraft flask-air sampling program located primarily over North America. The inversions derived from these flask-air measurements are referred to here as “flask-only inversions”. In this first base scenario, we used the same prior emission with a global CFC-11 emission of 67 Gg yr<sup>-1</sup> (“population 67” shown in Fig. 2) for both HIPPO and ATom periods (Table S1). The global emissions derived from this scenario (67 ± 7 Gg yr<sup>-1</sup> and 87 ± 9 Gg yr<sup>-1</sup> for the HIPPO and ATom periods) were based on background estimates that were calibrated against the global 3-box model results, such that the global CFC-11 emissions derived

Deleted: I  
 Deleted: IV  
 Deleted: III  
 Deleted: IV  
 Deleted: I  
 Deleted: IV  
 Deleted: similar in both periods

Deleted: ; but

Deleted: Subtracting the  
 Deleted: there were  
 Deleted: up to  
 Deleted: measured  
 Formatted: Font color: Auto  
 Deleted: the global  
 Deleted: –  
 Deleted: only  
 Deleted: were

Deleted:

Deleted: when comparing air over the Pacific Ocean versus the Atlantic Ocean sampled by  
 Formatted: Font color: Auto  
 Deleted: air above  
 Deleted: was more enhanced with CFC-11  
 Deleted: air above  
 Formatted: Font color: Auto  
 Deleted: may be emitted  
 Deleted: above

Deleted: ”

Deleted:

578 from the grid-scale inversions were consistent with those from the global 3-box model with an  
 579 atmospheric lifetime of 52 years reported by Montzka et al. (2021).

580 An inverse analysis of the flask data obtained during the HIPPO and ATom periods suggest  
 581 changes in the total magnitude and distribution of CFC-11 emissions from 2010 to  
 582 2018. Significant emission increases were derived for Asia, by an amount that suggests it was  
 583 primarily responsible for the global CFC-11 emission increase from 2010 to 2018. During the  
 584 HIPPO period (November 2009 – September 2011), Asia emitted 35 ( $\pm 5$ ) Gg yr<sup>-1</sup> of CFC-11,  
 585 accounting for 50% of global CFC-11 emissions, whereas Asian annual CFC-11 emissions  
 586 increased to 51 ( $\pm 8$ ) Gg yr<sup>-1</sup> during the ATom period in August 2016 – May 2018, equal to 60%  
 587 of the global CFC-11 emission at that time. Results from this scenario yield an increase of CFC-  
 588 11 emission from Asia during these two periods of 16 ( $\pm 10$ ) Gg yr<sup>-1</sup>, which accounted for 80 -  
 589 90 % of global CFC-11 emission increases during these specific years (19 + 12) (Fig. 6), as derived  
 590 from this scenario.

591 Our inversion results also suggest that the Asian CFC-11 emissions and emission increases  
 592 were primarily contributed by the temperate eastern Asia, temperate western Asia, and tropical  
 593 Asia in approximately equal amounts (Fig. 6). Correlations (as  $r^2$ ) or covariations in the posterior  
 594 emissions among these three Asian subregions, were less than 0.1, suggesting the inversion was  
 595 able to separate regional total emissions from these three subregions, although the derived  
 596 analytical uncertainties associated with emissions at the subregional level are overlapping (Fig. 6).

597 Emissions derived for North America, South America, Africa, and Europe were 5 – 15 Gg  
 598 yr<sup>-1</sup> for each region in both the HIPPO and ATom periods. Emissions derived for Australia were  
 599 less than 1 Gg yr<sup>-1</sup>. Changes of CFC-11 emissions between both periods derived for all seven of  
 600 these continents were smaller than their associated uncertainties in this scenario.

601 With “flask-only” observations, we also tested the sensitivity of posterior regional  
 602 emissions to the prior emission magnitude. Here, we considered the second “population-density”  
 603 prior with a substantially lower global total CFC-11 emission of 40 Gg yr<sup>-1</sup> for both periods  
 604 (“population\_40”) (Table S1). Derived regional emissions from this second scenario were  
 605 consistent with results discussed in the first scenario in both the distribution and total magnitude  
 606 of posterior emissions.

607 To assess how much constraint the selected atmospheric observations added to regional  
 608 emission estimates, we calculated the uncertainty reduction between the prior and posterior  
 609 emission uncertainties. Note that the uncertainty reduction is generally correlated with the  
 610 sensitivity of atmospheric observations to surface emissions (or footprint) and is dependent on how  
 611 good the prior emission is. As expected, the uncertainty reduction is indeed the largest (50 – 80%)  
 612 over North America and Asia (Table S2; Fig. 6), where our observations have the strongest  
 613 sensitivity, and the smallest over South America, Africa, and Australia (3 – 50%) (Fig. 6; Table  
 614 S2), where our observations have the lowest sensitivity (Fig. 1).

615  
 616 **3.2.2. Inversions using more observations, different prior assumptions, and an alternative**  
 617 **background mole fraction field**

618 To increase the observational constraints in the global CFC-11 inversion, we then included  
 619 additional observations from the in situ CFC-11 measurements (Fig. 1; Inversion ID = 3 – 4 in  
 620 Table S1). The derived posterior emissions with this expanded observational dataset (and with the  
 621 same population-based priors and background estimates) show slightly higher global emissions,  
 622 especially from tropical Asia, during the ATom period (Fig. 7). Besides inclusion of additional  
 623 observations, we also considered an alternative background estimate (background 2) that was

Deleted: , which we estimate

Deleted: The

Deleted: ,

Deleted: ( $r^2$ )

Deleted: regions

Deleted: large

Deleted:

Formatted: Font color: Black

Deleted: from this scenario

Formatted: Font color: Black

Deleted: Scenarios with

Deleted: -

Deleted: 1



635 calibrated to the global CFC-11 emission estimates with alternative atmospheric lifetimes (54 and  
 636 56 years) (Montzka et al., 2021) (Inversion ID = 5 in Table S1). As expected, the derived global  
 637 and regional emissions were lower with a background calibrated to a longer atmospheric lifetime.  
 638 However, the derived regional contributions to the global CFC-11 emissions and emission changes  
 639 between the HIPPO and ATom periods were consistent with results considering a shorter lifetime  
 640 (Fig. 7).

641 Results discussed so far are based on prior emissions that do not change between the  
 642 HIPPO and ATom periods for all regions considered. The remaining questions are: 1) are the  
 643 resulting near-zero emission changes over North America, South America, Africa, Europe, and  
 644 Australia due to the influence from prior assumption (zero emission changes in the prior) or are  
 645 they the result of observational constraints? and 2) to what degree are derived Asian emissions and  
 646 emission changes dependent on assumptions of prior emission changes? To address these  
 647 questions, we constructed 18 additional scenarios (as part of the 23 scenarios described in Section  
 648 2.2.5) that assumed 20 Gg yr<sup>-1</sup> CFC-11 emission increases in the prior emissions between the  
 649 HIPPO and ATom (Inversion ID = 6 - 14 in Table S1) or 20 Gg yr<sup>-1</sup> CFC-11 emission decreases  
 650 between the HIPPO and ATom periods (Inversion ID = 15 - 23 in Table S1). In the first 9 cases,  
 651 we considered the same population-based prior with a global CFC-11 emission of 67 Gg yr<sup>-1</sup> during  
 652 the HIPPO period (prior = "population 67"), whereas during the ATom period, we assumed there  
 653 was an increase of 20 Gg yr<sup>-1</sup> of CFC-11 emissions over individual continents (North America,  
 654 South America, Africa, Europe, Australia) or individual Asian subregions (boreal Asia, temperate  
 655 eastern Asia, temperate western Asia, and tropical Asia) (prior = "population 87 region"). In the  
 656 latter 9 cases, we considered opposite scenarios, where we assumed 67 Gg yr<sup>-1</sup> of emissions during  
 657 the ATom period (prior = "population 67") and 87 Gg yr<sup>-1</sup> of emissions during the HIPPO period,  
 658 (prior = "population 87 region"), so that emissions over individual continents or individual Asian  
 659 subregions had a 20 Gg yr<sup>-1</sup> decrease between both periods (Fig. 8). Note that, given it is known  
 660 there was a global increase of CFC-11 emissions from 2010 to 2018 (Montzka et al., 2021;  
 661 Montzka et al., 2018) and 60 ± 40 % of this global increase was from eastern mainland China (Park  
 662 et al., 2021; Rigby et al., 2019), many of the assumed 18 prior emission change cases were quite  
 663 unrealistic. However, such extreme cases helped for estimating uncertainties that truly reflect the  
 664 capability of the selected atmospheric measurements for constraining continental and regional  
 665 emissions and their change through time. In all of the 18 extreme cases, regional emissions and  
 666 emission changes derived for the northern hemispheric lands, i.e., Asia, North America, Europe,  
 667 were consistent (Fig. 8). Derived regional emissions and emission changes for the southern  
 668 hemispheric lands, such as South America, Africa, Australia, however, show a strong dependence  
 669 on prior assumptions, especially during the ATom period (Fig. 8). The strong dependence of  
 670 inversion-derived emissions over the southern hemispheric lands were due to large sampling gaps  
 671 and small sensitivity to emissions from these regions (Fig. 1).

672 Summarizing emissions derived from all 23 inversion ensembles (Table 1; Figs. 6 - 8), our  
 673 results suggest the relatively remote observations provide important constraints on regional  
 674 emissions from North America, Asia, and Europe, as the derived ranges of posterior emissions  
 675 were smaller than the ranges of prior emissions considered for these regions (Figs. 6 - 8). The  
 676 only continent that shows a statistically significant increase of CFC-11 emissions is Asia, where  
 677 the best estimate of these 23 cases suggests an increase of 24 (18 - 28) Gg yr<sup>-1</sup> of CFC-11 emissions  
 678 (the 2.5<sup>th</sup> - 97.5<sup>th</sup> percentile range) (Table 1), accounting for 86 (59 - 115) % of the global CFC-  
 679 11 emission increases between the HIPPO and ATom periods. All the best estimates from the 23  
 680 inversion ensembles suggest CFC-11 emission increases not only from temperate eastern Asia, but

- Deleted: were
- Deleted: with zero changes
- Deleted: whether
- Formatted: Font color: Auto
- Deleted: derived
- Deleted: were
- Deleted: of
- Deleted: if
- Formatted: Font color: Auto
- Deleted: were constrained by the atmospheric observations. Another question is how much the
- Deleted: are
- Deleted: prior
- Deleted: .
- Deleted: 14
- Deleted: emission priors
- Formatted: Font color: Black
- Deleted: 7 priors
- Deleted: both
- Deleted: another 7 priors;
- Deleted: ; Fig. 8
- Deleted: 7
- Deleted: ,
- Deleted: i.e.,
- Deleted: i.e.,
- Deleted: Table S1; Fig. 8).
- Deleted: 7
- Deleted: ,
- Deleted: we've already know
- Deleted: 14
- Deleted: 14
- Deleted: .

710 also from temperate western Asia and tropical Asia. However, if we consider the entire range of  
 711 uncertainties (the range of best estimates and  $2\sigma$  errors from each inversion: Table 1), the derived  
 712 emission increases were statistically insignificant at the subregion level (i.e., temperate eastern  
 713 Asia, temperate western Asia, and tropical Asia).

714 Our results also suggest inverse modeling of the relatively remote observations we  
 715 considered here provided only weak constraints on emissions from the southern hemispheric  
 716 continents, i.e., South America, Africa, and Australia. Although we cannot eliminate the  
 717 possibility of some increase in CFC-11 emissions from these southern hemispheric regions based  
 718 on atmospheric inversion analyses alone, they did not account for the majority of the emission  
 719 increase. This is because during 2010 – 2018, when the global CFC-11 emissions increased, so  
 720 did the north-to-south mole fraction difference between the hemispheres (Montzka et al., 2021),  
 721 which indicates the emission increase occurred predominantly in the northern hemisphere.

### 722 3.2.3. Comparison of regional emission estimates from other top-down analyses

723 Our regional emission estimates of CFC-11 from the global atmospheric CFC-11  
 724 measurements made far away from the emissive regions are in a broad agreement with those  
 725 estimated from atmospheric observations made closely downwind of the emissive regions (Table  
 726 2), which included the analyses of atmospheric CFC-11 enhancements observed closely downwind  
 727 of emissive regions that were one-two orders of magnitude larger than those used in the present  
 728 inversion analysis (Park et al., 2021; Rigby et al., 2019; Hu et al., 2017; Fraser et al., 2020).  
 729 Emissions estimated for eastern mainland China using measurements made in South Korea were  
 730  $5 - 13 \text{ Gg yr}^{-1}$  during 2010 – 2011 and  $12 - 20 \text{ Gg yr}^{-1}$  during 2016 - 2017, considering the full  
 731 range of estimates from multiple inversion systems with different transport simulations (Park et  
 732 al., 2021). CFC-11 emission estimates for eastern China based on measurements made in Taiwan  
 733 were  $14 - 23 \text{ Gg yr}^{-1}$  during 2014 – 2018 (Adcock et al., 2020). In the current analysis, we  
 734 estimated CFC-11 emissions from temperate eastern Asia were  $5 - 16 \text{ Gg yr}^{-1}$  during Nov 2009 –  
 735 Sep 2011 and  $9 - 22 \text{ Gg yr}^{-1}$  during August 2016 – May 2018, which agree well with the published  
 736 analyses over eastern China, although our definition of temperate eastern Asia is slightly different  
 737 from the regions defined in Rigby et al. (2019), Adcock et al. (2020) and Park et al. (2021).

738 Previously, we estimated the US emissions of CFC-11 between 2008 and 2014 with more  
 739 extensive atmospheric measurements made from towers and aircraft sites from all vertical levels  
 740 over North America (Hu et al., 2017). In this analysis, we only used a subset of observations (only  
 741 aircraft observations above 1 km above ground) and a coarser resolution of transport models in the  
 742 global inversion. While the North American CFC-11 emissions derived here are likely not as  
 743 accurate, they did agree within uncertainties with our previous US estimates (Table 2).

744 Furthermore, CFC-11 emissions derived for Australia are also comparable with estimates  
 745 reported by Fraser et al. (2020) using measurements made in Australia (Table 2). Both suggest  
 746 CFC-11 emissions from Australia were less than  $1 \text{ Gg yr}^{-1}$  between 2009 and 2018, and  
 747 contributions from Australia to global CFC-11 emissions and emission changes were very small.

748 Besides temperate eastern Asia, North America, and Australia, we also compared our  
 749 derived European CFC-11 emissions for Nov 2009 – Sep 2011 with the value reported by Keller  
 750 et al. (2011) for western Europe in 2009. Our best estimate of  $4.2 (2.9 - 5.4) \text{ Gg yr}^{-1}$  for all of  
 751 Europe was about twice as large as reported by Keller et al. (2011) for the western Europe, which  
 752 only accounted for 40% of the area we considered for all of Europe. If aggregating emissions from  
 753 only grid cells considered in Keller et al. (2011), the aggregated total emissions would be similar  
 754

Deleted:  $2\sigma$

Deleted: had

Formatted: Font color: Auto

Deleted: this

Deleted: ;

Deleted: . Contributions

Formatted: Font color: Auto

760 to the value reported by Keller et al. (2011), although both studies focused on two different time  
 761 periods (Table 2).

762 Other than the regions mentioned above, previous emission estimates for the rest of the  
 763 world are quite limited. Only one study quantified CFC-11 emissions from the northern and central  
 764 areas of India in June 2016, reporting emissions of  $\sim 1 - 3 \text{ Gg yr}^{-1}$  (Say et al., 2019). It is hard to  
 765 make a fair comparison with our analysis, given its short analysis period and a much smaller area  
 766 than our defined temperate western Asian region (Fig. 4). However, there is observational  
 767 evidence indicating likely strong regional emissions and a regional emission increase over  
 768 temperate western Asia between 2012 – 2017. This was shown as substantially enhanced CFC-11  
 769 mole fractions observed in temperate western Asia for flask measurements made during 2012 –  
 770 2018 (Simpson et al., 2019) and the slow-down of atmospheric CFC-11 decline retrieved from  
 771 satellite remote sensing measurements (Chen et al., 2020). Furthermore, in situ measurements  
 772 made in tropical Asia in 2017 (Lin et al., 2019) also indicate likely strong regional emissions of  
 773 CFC-11 over this area.

774 **4. Conclusions**

775 We used global atmospheric CFC-11 measurements primarily made over the Pacific and  
 776 Atlantic Ocean basins and in the free troposphere over North America to quantify changes in  
 777 continental-scale emissions between November 2009 - September 2011 and August 2016 – May  
 778 2018. These two periods covered the times when global CFC-11 emissions were at their minimum  
 779 and maximum, respectively, in recent years, at least before the sharp decline noted after 2018  
 780 (Montzka et al., 2021). Atmospheric CFC-11 measurements made during both the HIPPO and  
 781 ATom campaigns confirm that the slow-down of atmospheric CFC-11 mole fraction decline  
 782 between 2009 and 2018 was present throughout the troposphere. The ATom campaign data further  
 783 display larger atmospheric CFC-11 enhancements in flights, particularly over the Pacific Ocean  
 784 basin as compared to the Atlantic Ocean basin, suggesting larger emissions in regions immediately  
 785 upwind of the Pacific Ocean than the Atlantic Ocean during 2016-2018.

786 Inverse modeling of these global atmospheric CFC-11 measurements suggests three Asian  
 787 regions were primarily responsible for the global CFC-11 emission changes from 2009-11 to 2016-  
 788 18 in all of the 23 inversion ensembles, including various extreme initial assumptions of regional  
 789 CFC-11 emission changes ( $\pm 20 \text{ Gg yr}^{-1}$ ) between both periods. Our results suggest that, during  
 790 November 2009 – September 2011, Asia emitted 24 (14 – 40)  $\text{Gg yr}^{-1}$  of CFC-11, accounting for  
 791 43 (37 – 52) % of the global emission (Table 1), whereas the Asian CFC-11 emissions increase to  
 792 48 (38 – 65)  $\text{Gg yr}^{-1}$  or 57 (49 - 62) % of the global emission during August 2016 – May 2018  
 793 (Table 1). In both periods, substantial CFC-11 emissions were derived for temperate eastern Asia,  
 794 temperate western Asia, and tropical Asia. Besides eastern mainland China, our results suggest  
 795 there could be increases of CFC-11 emissions from temperate western Asia and tropical Asia from  
 796 2010 to 2018, considering the range of best estimates from the 23 inversion ensembles. In contrast  
 797 to Asia, other continents accounted for relatively smaller fractions of global CFC-11 emissions in  
 798 both periods. For continents in the Southern Hemisphere, our inversion analyses only provide weak  
 799 constraints on the CFC-11 emission changes between 2012 and 2018. However, significant  
 800 increases in CFC-11 emissions from these regions are unlikely, provided the observed concurrent  
 801 increase of the north-to-south difference in CFC-11 surface mole fractions.

802 **Acknowledgement**

- Deleted: area
- Deleted: In temperate western Asia and tropical Asia
- Deleted: was
- Formatted: Font color: Auto
- Formatted: Font color: Auto
- Deleted: -
- Deleted: , which were
- Deleted: in
- Deleted: in tropical Asia for
- Deleted: )

- Deleted: the
- Deleted: in
- Formatted: Font color: Auto

- Deleted: Although for
- Deleted: given

817 This work was funded by the NASA Earth Venture Atmospheric Tomography (ATom) mission  
818 (NNX16AL92A) and in part by the NOAA Cooperative Agreement with CIRES,  
819 NA17OAR4320101. We thank our retired colleagues Dr. Ben Miller for his development of the  
820 Perseus (PR1) GCMS instrument and Dr. James Elkins for his leadership and contribution to the  
821 HIPPO and ATom flask sampling and measurements. We also thank Dr. Arlyn Andrews, Dr. Ariel  
822 Stein, and Dr. Christopher Loughner for suggestions on HYSPLIT simulations.

823 **Code/Data availability:** NOAA atmospheric observations are available at the NOAA/GML  
824 website (<https://gml.noaa.gov/hats/>). Data collected from ATom are available via  
825 <https://espo.nasa.gov/atom/content/ATom> and <https://doi.org/10.3334/ORNLDAAAC/1581>. Data  
826 collected from HIPPO are available via  
827 [https://www.nsf.gov/news/news\\_summ.jsp?cntn\\_id=127003](https://www.nsf.gov/news/news_summ.jsp?cntn_id=127003). Inversion-derived continental  
828 fluxes were tabulated and described in this paper. All analysis tools and computing code used in  
829 this analysis will be available by contacting LH ([lei.hu@noaa.gov](mailto:lei.hu@noaa.gov)).

### 831 Author contributions

832 LH and SAM designed the analysis; LH conducted inversions and wrote the paper; SAM led the  
833 NOAA global flask measurements, HIPPO and ATom GCMS measurements, and provided  
834 substantial input on the analyses and edits of this paper; FM and EH collected HIPPO and ATom  
835 flask-air samples; GD led the CATS measurements and prepared CATS data for this analysis;  
836 MCS made the NOAA flask measurements; LH and KT computed HYSPLIT footprints; RWP  
837 conducted the WACCM simulations and provided the model results; KM conducted NOAA  
838 aircraft data QA/QC; CW led the NOAA aircraft sampling network; IV led the Persus GCMS flask  
839 measurements; DN helped with data QA/QC for CFC-11 flask measurements; BH led the  
840 calibration for NOAA measurements; SW led the HIPPO and ATom campaigns; all authors  
841 contributed to the editing of this paper.

842 **Competing interests:** the authors declare no competing interests.

### 843 References

844 Adcock, K. E., Ashfold, M. J., Chou, C. C. K., Gooch, L. J., Mohd Hanif, N., Laube, J. C., Oram,  
845 D. E., Ou-Yang, C.-F., Panagi, M., Sturges, W. T., and Reeves, C. E.: Investigation of East Asian  
846 Emissions of CFC-11 Using atmospheric observations in Taiwan, *Environmental Science &*  
847 *Technology*, 54, 3814-3822, 10.1021/acs.est.9b06433, 2020.

848 Bourgeois, I., Peischl, J., Thompson, C. R., Aikin, K. C., Campos, T., Clark, H., Commane, R.,  
849 Daube, B., Diskin, G. W., Elkins, J. W., Gao, R. S., Gaudel, A., Hints, E. J., Johnson, B. J., Kivi,  
850 R., McKain, K., Moore, F. L., Parrish, D. D., Querel, R., Ray, E., Sánchez, R., Sweeney, C.,  
851 Tarasick, D. W., Thompson, A. M., Thouret, V., Witte, J. C., Wofsy, S. C., and Ryerson, T. B.:  
852 Global-scale distribution of ozone in the remote troposphere from the ATom and HIPPO airborne  
853 field missions, *Atmos. Chem. Phys.*, 20, 10611-10635, 10.5194/acp-20-10611-2020, 2020.

854 Chen, X., Huang, X., and Strow, L. L.: Near-Global CFC-11 trends as observed by Atmospheric  
855 Infrared Sounder From 2003 to 2018, *Journal of Geophysical Research: Atmospheres*, 125,  
856 e2020JD033051, <https://doi.org/10.1029/2020JD033051>, 2020.

Deleted: ).

Deleted: (<https://gml.noaa.gov/hats/>).

Deleted: were

Deleted: <https://espo.nasa.gov/atom/content/ATom>.

Deleted: were

Deleted: [https://www.nsf.gov/news/news\\_summ.jsp?cntn\\_id=127003](https://www.nsf.gov/news/news_summ.jsp?cntn_id=127003).

Formatted: Pattern: Clear, Highlight

Deleted: upon reasonable request.

Formatted: Pattern: Clear, Highlight

Deleted: Atmospheric Observations

Deleted: Trends

Deleted: Observed

Deleted: <https://doi.org/10.1029/2020JD033051>,

- 872 Davis, N. A., Davis, S. M., Portmann, R. W., Ray, E., Rosenlof, K. H., and Yu, P.: A  
873 comprehensive assessment of tropical stratospheric upwelling in the specified dynamics  
874 Community Earth System Model 1.2.2 – Whole Atmosphere Community Climate Model (CESM  
875 (WACCM)), *Geosci. Model Dev.*, 13, 717-734, 10.5194/gmd-13-717-2020, 2020.
- 876 Dhomse, S. S., Feng, W., Montzka, S. A., Hossaini, R., Keeble, J., Pyle, J. A., Daniel, J. S., and  
877 Chipperfield, M. P.: Delay in recovery of the Antarctic ozone hole from unexpected CFC-11  
878 emissions, *Nature Communications*, 10, 5781, 10.1038/s41467-019-13717-x, 2019.
- 879 Engel, A., Rigby, M., Burkholder, J. B., Fernandez, R. P., Froidevaux, L., Hall, B. D., Hossaini,  
880 R., Saito, T., Vollmer, M. K., and Yao, B.: Update on Ozone-Depleting Substances (ODSs) and  
881 Other Gases of Interest to the Montreal Protocol, Chapter 1 in *Scientific Assessment of Ozone  
882 Depletion: 2018*, World Meteorological Organization, Geneva, Switzerland, 2018.
- 883 Fraser, P. J., Dunse, B. L., Krummel, P. B., Steele, L. P., Derek, N., Mitrevski, B., Allison, C. E.,  
884 Loh, Z., Manning, A. J., Redington, A., and Rigby, M.: Australian chlorofluorocarbon (CFC)  
885 emissions: 1960–2017, *Environmental Chemistry*, 17, 525-544, <https://doi.org/10.1071/EN19322>,  
886 2020.
- 887 Hu, L., Montzka, S. A., Lehman, S. J., Godwin, D. S., Miller, B. R., Andrews, A. E., Thoning, K.,  
888 Miller, J. B., Sweeney, C., Siso, C., Elkins, J. W., Hall, B. D., Mondeel, D. J., Nance, D., Nehrkorn,  
889 T., Mountain, M., Fischer, M. L., Biraud, S. C., Chen, H., and Tans, P. P.: Considerable  
890 contribution of the Montreal Protocol to declining greenhouse gas emissions from the United  
891 States, *Geophysical Research Letters*, 44, 2017GL074388, 10.1002/2017GL074388, 2017.
- 892 Hu, L., Montzka, S. A., Miller, B. R., Andrews, A. E., Miller, J. B., Lehman, S. J., Sweeney, C.,  
893 Miller, S. M., Thoning, K., Siso, C., Atlas, E. L., Blake, D. R., de Gouw, J., Gilman, J. B., Dutton,  
894 G., Elkins, J. W., Hall, B., Chen, H., Fischer, M. L., Mountain, M. E., Nehrkorn, T., Biraud, S. C.,  
895 Moore, F. L., and Tans, P.: Continued emissions of carbon tetrachloride from the United States  
896 nearly two decades after its phaseout for dispersive uses, *Proceedings of the National Academy of  
897 Sciences*, 113, 2880-2885, 10.1073/pnas.1522284113, 2016.
- 898 Hu, L., Montzka, S. A., Miller, J. B., Andrews, A. E., Lehman, S. J., Miller, B. R., Thoning, K.,  
899 Sweeney, C., Chen, H., Godwin, D. S., Masarie, K., Bruhwiler, L., Fischer, M. L., Biraud, S. C.,  
900 Torn, M. S., Mountain, M., Nehrkorn, T., Eluszkiewicz, J., Miller, S., Draxler, R. R., Stein, A. F.,  
901 Hall, B. D., Elkins, J. W., and Tans, P. P.: U.S. emissions of HFC-134a derived for 2008–2012  
902 from an extensive flask-air sampling network, *Journal of Geophysical Research: Atmospheres*,  
903 2014JD022617, 10.1002/2014JD022617, 2015.
- 904 Keeble, J., Abraham, N. L., Archibald, A. T., Chipperfield, M. P., Dhomse, S., Griffiths, P. T., and  
905 Pyle, J. A.: Modelling the potential impacts of the recent, unexpected increase in CFC-11  
906 emissions on total column ozone recovery, *Atmos. Chem. Phys.*, 20, 7153-7166, 10.5194/acp-20-  
907 7153-2020, 2020.
- 908 Keller, C. A., Brunner, D., Henne, S., Vollmer, M. K., O'Doherty, S., and Reimann, S.: Evidence  
909 for under-reported western European emissions of the potent greenhouse gas HFC-23,  
910 *Geophysical Research Letters*, 38, L15808, 10.1029/2011gl047976, 2011.
- 911 Lin, Y., Gong, D., Lv, S., Ding, Y., Wu, G., Wang, H., Li, Y., Wang, Y., Zhou, L., and Wang, B.:  
912 Observations of High Levels of Ozone-Depleting CFC-11 at a Remote Mountain-Top Site in

Deleted: <https://doi.org/10.1071/EN19322>.



- 914 Southern China, *Environmental Science & Technology Letters*, 6, 114-118,  
915 10.1021/acs.estlett.9b00022, 2019.
- 916 Marsh, D. R., Mills, M. J., Kinnison, D. E., Lamarque, J.-F., Calvo, N., and Polvani, L. M.: Climate  
917 Change from 1850 to 2005 Simulated in CESM1(WACCM), *Journal of Climate*, 26, 7372-7391,  
918 10.1175/jcli-d-12-00558.1, 2013.
- 919 Michalak, A. M., Hirsch, A., Bruhwiler, L., Gurney, K. R., Peters, W., and Tans, P. P.: Maximum  
920 likelihood estimation of covariance parameters for Bayesian atmospheric trace gas surface flux  
921 inversions, *Journal of Geophysical Research: Atmospheres*, 110, D24107, 10.1029/2005jd005970,  
922 2005.
- 923 Montzka, S. A., Dutton, G. S., Yu, P., Ray, E., Portmann, R. W., Daniel, J. S., Kuijpers, L., Hall,  
924 B. D., Mondeel, D., Siso, C., Nance, J. D., Rigby, M., Manning, A. J., Hu, L., Moore, F., Miller,  
925 B. R., and Elkins, J. W.: An unexpected and persistent increase in global emissions of ozone-  
926 depleting CFC-11, *Nature*, 557, 413-417, 10.1038/s41586-018-0106-2, 2018.
- 927 **Montzka, S. A., Dutton, G. S., Portmann, R. W., Chipperfield, M. P., Davis,**  
928 **S., Feng, W., Manning, A. J., Ray, E., Rigby, M., Hall, B. D., Siso, C., Nance,**  
929 **J. D., Krummel, P. B., Mühle, J., Young, D., O'Doherty, S., Salameh, P. K.,**  
930 **Harth, C. M., Prinn, R. G., Weiss, R. F., Elkins, J. W., Walter-Terrinoni, H.,**  
931 **and Theodoridi, C.: A decline in global CFC-11 emissions during**  
932 **2018–2019, *Nature*, 590, 428–432, 10.1038/s41586-021-03260-5, 2021.**
- 933 Nehr Korn, T., Eluszkiewicz, J., Wofsy, S., Lin, J., Gerbig, C., Longo, M., and Freitas, S.: Coupled  
934 weather research and forecasting–stochastic time-inverted lagrangian transport (WRF–STILT)  
935 model, *Meteorology and Atmospheric Physics*, 107, 51-64, 10.1007/s00703-010-0068-x, 2010.
- 936 Park, S., Western, L. M., Saito, T., Redington, A. L., Henne, S., Fang, X., Prinn, R. G., Manning,  
937 A. J., Montzka, S. A., Fraser, P. J., Ganesan, A. L., Harth, C. M., Kim, J., Krummel, P. B., Liang,  
938 Q., Mühle, J., O'Doherty, S., Park, H., Park, M.-K., Reimann, S., Salameh, P. K., Weiss, R. F.,  
939 and Rigby, M.: A decline in emissions of CFC-11 and related chemicals from eastern China,  
940 *Nature*, 590, 433-437, 10.1038/s41586-021-03277-w, 2021.
- 941 Ray, E. A., Portmann, R. W., Yu, P., Daniel, J., Montzka, S. A., Dutton, G. S., Hall, B. D., Moore,  
942 F. L., and Rosenlof, K. H.: The influence of the stratospheric Quasi-Biennial Oscillation on trace  
943 gas levels at the Earth's surface, *Nature Geoscience*, 13, 22-27, 10.1038/s41561-019-0507-3,  
944 2020.
- 945 Rigby, M., Park, S., Saito, T., Western, L. M., Redington, A. L., Fang, X., Henne, S., Manning,  
946 A. J., Prinn, R. G., Dutton, G. S., Fraser, P. J., Ganesan, A. L., Hall, B. D., Harth, C. M., Kim, J.,  
947 Kim, K. R., Krummel, P. B., Lee, T., Li, S., Liang, Q., Lunt, M. F., Montzka, S. A., Mühle, J.,  
948 O'Doherty, S., Park, M. K., Reimann, S., Salameh, P. K., Simmonds, P., Tunnicliffe, R. L., Weiss,  
949 R. F., Yokouchi, Y., and Young, D.: Increase in CFC-11 emissions from eastern China based on  
950 atmospheric observations, *Nature*, 569, 546-550, 10.1038/s41586-019-1193-4, 2019.
- 951 Rodgers, C. D.: *Inverse Methods for Atmospheric Sounding*, World Sci., Oxford, 10.1142/3171,  
952 2000.

953 Say, D., Ganesan, A. L., Lunt, M. F., Rigby, M., O'Doherty, S., Harth, C., Manning, A. J.,  
954 Krummel, P. B., and Bauguitte, S.: Emissions of halocarbons from India inferred through  
955 atmospheric measurements, *Atmos. Chem. Phys.*, 19, 9865-9885, 10.5194/acp-19-9865-2019,  
956 2019.

957 Simpson, I. J., Blake, D. R., Barletta, B., Meinardi, S., Blake, N. J., Wang, T., Yang, L., Stone, E.  
958 A., Yokelson, R. J., Farrukh, M. A., Aburizaiza, O. S., Khwaja, H., Siddique, A., Zeb, J., Woo, J.  
959 H., Kim, Y., Diskin, G. S., and Peterson, D. A.: Recent CFC-11 Enhancements in China, Nepal,  
960 Pakistan, Saudi Arabia and South Korea, American Geophysical Union, Fall Meeting 2019, San  
961 Francisco, CO, USA, December 01, 2019, 2019AGUFM.A33T2896S, A33T-2896, 2019.

962 Stein, A. F., Draxler, R. R., Rolph, G. D., Stunder, B. J. B., Cohen, M. D., and Ngan, F.: NOAA's  
963 HYSPLIT atmospheric transport and dispersion modeling system, *Bulletin of the American  
964 Meteorological Society*, 10.1175/BAMS-D-14-00110.1, 2015.

965 United Nations Environment Programme (UNEP): Executive Committee of the Multilateral Fund  
966 for the Implementation of the Montreal Protocol, Eighty-third Meeting. Addendum: Reports On  
967 Projects With Specific Reporting Requirements., 2019.

968 United Nations Environment Programme (UNEP): Consumption of controlled substances  
969 [dataset], 2021a.

970 United Nations Environment Programme (UNEP): Production of controlled substances [dataset],  
971 2021b.

972 Wofsy, S. C., S. Afshar, H.M. Allen, E.C. Apel, E.C. Asher, B. Barletta, J. Bent, H. Bian, B.C.  
973 Biggs, D.R. Blake, N. Blake, I. Bourgeois, C.A. Brock, W.H. Brune, J.W. Budney, T.P. Bui, A.  
974 Butler, P. Campuzano-Jost, C.S. Chang, M. Chin, R. Commane, G. Correa, J.D. Crouse, P. D.  
975 Cullis, B.C. Daube, D.A. Day, J.M. Dean-Day, J.E. Dibb, J.P. DiGangi, G.S. Diskin, M. Dollner,  
976 J.W. Elkins, F. Erdesz, A.M. Fiore, C.M. Flynn, K.D. Froyd, D.W. Gesler, S.R. Hall, T.F. Hanisco,  
977 R.A. Hannun, A.J. Hills, E.J. Hints, A. Hoffman, R.S. Hornbrook, L.G. Huey, S. Hughes, J.L.  
978 Jimenez, B.J. Johnson, J.M. Katich, R.F. Keeling, M.J. Kim, A. Kupc, L.R. Lait, J.-F. Lamarque,  
979 J. Liu, K. McKain, R.J. McLaughlin, S. Meinardi, D.O. Miller, S.A. Montzka, F.L. Moore, E.J.  
980 Morgan, D.M. Murphy, L.T. Murray, B.A. Nault, J.A. Neuman, P.A. Newman, J.M. Nicely, X.  
981 Pan, W. Paplawsky, J. Peischl, M.J. Prather, D.J. Price, E.A. Ray, J.M. Reeves, M. Richardson,  
982 A.W. Rollins, K.H. Rosenlof, T.B. Ryerson, E. Scheuer, G.P. Schill, J.C. Schroder, J.P. Schwarz,  
983 J.M. St.Clair, S.D. Steenrod, B.B. Stephens, S.A. Strode, C. Sweeney, D. Tanner, A.P. Teng, A.B.  
984 Thames, C.R. Thompson, K. Ullmann, P.R. Veres, N. Vieznor, N.L. Wagner, A. Watt, R. Weber,  
985 B. Weinzierl, P.O. Wennberg, C.J. Williamson, J.C. Wilson, G.M. Wolfe, C.T. Woods, and L.H.  
986 Zeng: ATom: Merged Atmospheric Chemistry, Trace Gases, and Aerosols [dataset],  
987 <https://doi.org/10.3334/ORNLDAAC/1581>, 2018.

988  
989  
990  
991  
992  
993  
994  
995

Deleted: <https://doi.org/10.3334/ORNLDAAC/1581>.

Deleted: ¶

Formatted: Font: Not Bold

Formatted: Indent: Left: 0", Hanging: 0.2"

**Table 1.** Global and regional emissions (Gg yr<sup>-1</sup>) derived from this analysis for Nov 2009 – Sep 2011 and Aug 2016 – May 2018 and the derived emission increases between the two periods (left columns). Two types of uncertainties were given in the parentheses. The former range indicates the 2.5<sup>th</sup> – 97.5<sup>th</sup> percentile range of the mean estimates derived from the 23 inversion ensembles. The latter range indicates the 2.5<sup>th</sup> – 97.5<sup>th</sup> percentile range of the 23 inversions, considering the mean and 2σ errors from each inversion. The right columns indicate the percentage contributions of regional emission to the global CFC-11 emissions and emission changes; values in the parentheses indicate the 2.5<sup>th</sup> – 97.5<sup>th</sup> percentile range of the mean regional emissions relative to the mean global emissions among the 23 inversion ensembles.

Region	Nov 2009 - Sep 2011		Aug 2016 - May 2018		Change	
	Emissions	Percentage	Emissions	Percentage	Emissions	Percentage
<b>Global</b>	56 (49 – 68; 39 - 75)	100	84 (78 – 101; 67 – 113)	100	29 (21 – 40; 5 – 56)	100
<b>Continents</b>						
N. America	5.9 (5.6 – 7.1; 4.4 - 8.5)	11 (9 - 14)	5.6 (5.1 – 7.5; 3.5 – 9.6)	7 (6 - 9)	-0.4 (-2 – 1; -4 - 4)	-1 (-5 - 5)
S. America	6 (5 – 10; 1 - 16)	11 (9 - 16)	9 (7 – 18; 3 - 25)	11 (8 - 18)	3 (-2 – 11; -9 – 19)	8 (-9 - 27)
Africa	10 (7 – 14; 1 - 23)	17 (13 - 24)	9 (7 – 14; 2 - 24)	11 (8 - 15)	-1 (-6 – 5; -17 – 15)	-3 (-26 - 14)
Asia	24 (21 – 33; 14 - 40)	43 (37 - 52)	48 (45 – 56; 38 - 65)	57 (49 - 62)	24 (18 – 28; 8 - 39)	86 (59 - 115)
Europe	9 (5 – 11; 2 - 15)	15 (11 - 20)	11 (7 – 15; 4 - 18)	12 (9 - 16)	2 (-2 – 5; -7 - 10)	7 (-7 - 19)
Australia	0.5 (0.4 – 2; -1 - 4)	1 (1-3)	1 (0.6 – 6; 0.1 - 10)	1 (1-7)	0.7 (-1 – 6; -4 - 11)	2 (-4 - 16)
<b>Asian Subregions</b>						
Boreal Asia	0.6 (0.2 – 3; 0.1 - 5)	1 (0 - 6)	0.8 (0.4 – 3; 0.1 - 4)	1 (0 - 3)	0.1 (-3 – 2; -4 - 4)	0 (-11 - 8)
Temperate E. Asia	10 (8 – 13; 5 – 16)	18 (15 - 21)	14 (12 – 18; 9 - 22)	17 (14 - 23)	4 (2 – 8; -3 - 12)	15 (6 - 34)
Temperate W. Asia	6 (4 – 10; -3 - 16)	10 (7 - 14)	16 (12 – 20; 5 - 29)	19 (15 - 23)	10 (6 – 13; -3 - 24)	36 (25 - 56)
Tropical Asia	8 (6 – 11; 2 - 16)	14 (11 - 18)	18 (16 – 23; 11 - 29)	21 (17 - 25)	10 (5 - 14; -2 - 22)	35 (22 - 51)

Deleted: best  
 Deleted: best estimates with their  
 Deleted: analytical uncertainties  
 Deleted: ensemble member.  
 Deleted: fractional  
 Deleted: . Values  
 Deleted: for the right columns  
 Deleted: from  
 Deleted: Definitions of various regions are shown in Fig. 3.

Deleted: :-

Deleted: ¶

Formatted: Left  
 Formatted: Font: Not Bold

1031  
1032

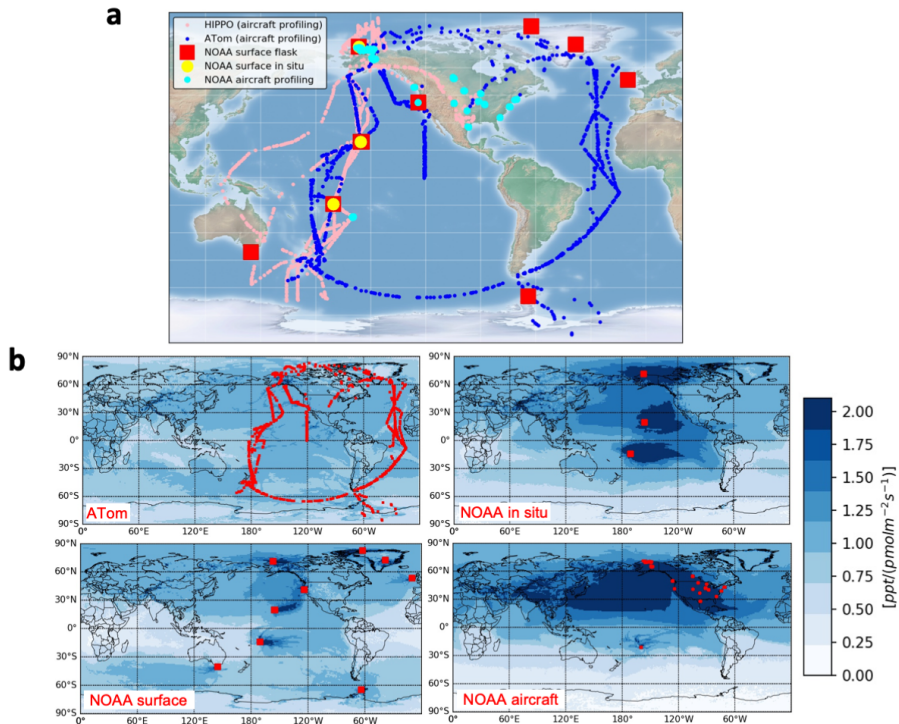
1053 **Table 2.** Comparison of regional emissions derived from this study and reported by previous top-  
 1054 down analyses.

Regions	Time Periods	Emissions (Gg/y)	References
<i>Asia</i>			
Eastern Mainland China	2008 - 2012	5 – 13 <sup>1</sup>	Rigby et al., 2019; Park et al., 2021
Temperate Eastern Asia	Nov 2009 - Sep 2011	10 (5 - 16)	This Study
Eastern Mainland China	2014 - 2017	12 – 20 <sup>1</sup>	Rigby et al., 2019; Park et al., 2021
Eastern China	2014 - 2018	19 ± 5	Adcock et al., 2020
Temperate Eastern Asia	Aug 2016 - May 2018	14 (9 - 22)	This Study
<i>Europe</i>			
35° - 55°N; -10° - 30°E	2009	4.2 (2.9 - 5.4)	Keller et al., 2011
35° - 70°N; -10° - 60°E	Nov 2009 - Sep 2011	10 (6 - 16)	This Study
<i>Australia</i>			
Australia	2010 - 2017	0.32 ± 0.04	Fraser et al., 2021
Australia	Nov 2009 - Sep 2011	0.4 (0 - 0.8)	This study
Australia	Aug 2016 - May 2018	0.6 (0.1 - 1.6)	This study
<i>North America</i>			
The contiguous US	2009 - 2011	8.2 ± 1.0	Hu et al., 2017
North America	Nov 2009 - Sep 2011	5.9 (4.4 - 8.5)	This study
The contiguous US	2014	4.5 ± 0.7	Hu et al., 2017
North America	Aug 2016 - May 2018	5.6 (3.5 - 9.6)	This study

Notes: <sup>1</sup>values were taken from the reported inversion ensemble spread.

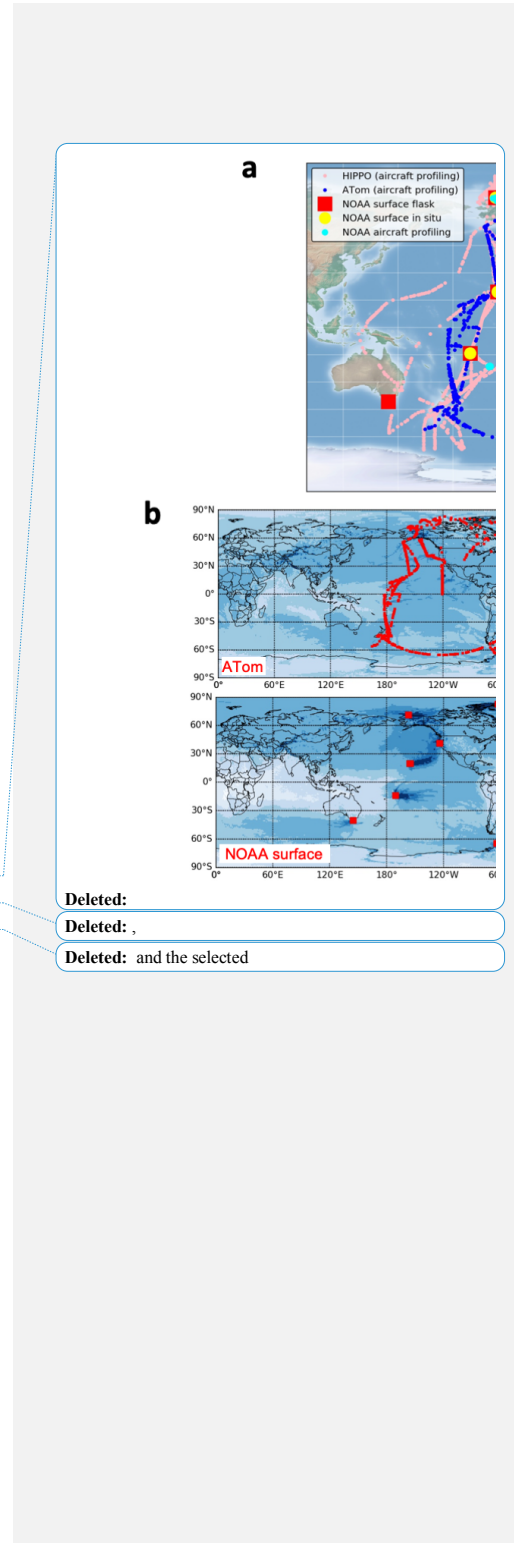
Formatted Table

1055  
1056  
1057  
1058  
1059  
1060  
1061  
1062  
1063  
1064  
1065  
1066  
1067  
1068  
1069

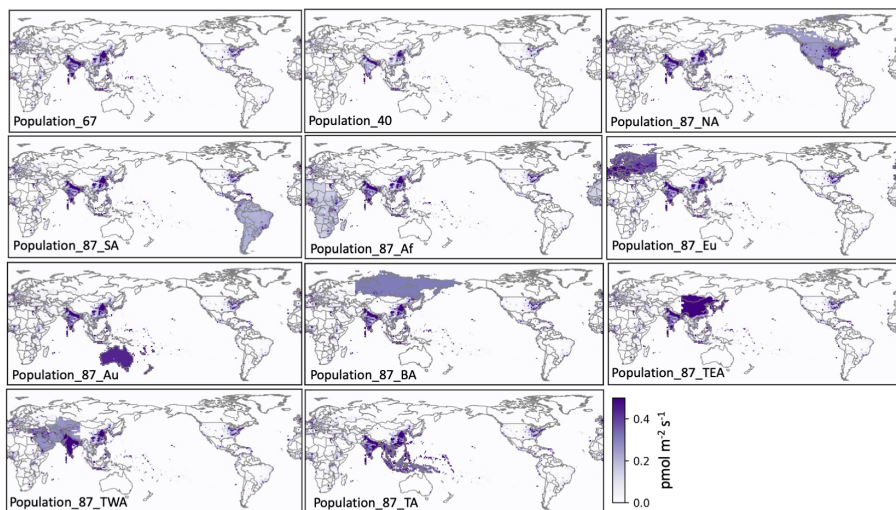


**Fig. 1.** Global atmospheric CFC-11 observations considered in this study (upper panel), including selected flask measurements from the NASA HIPPO and ATom campaigns, observations from the NOAA global weekly surface flask sampling network, NOAA global in situ surface sampling network, and NOAA aircraft profiling sites. The bottom four panels indicate the summed footprints between Aug 2016 – May 2018 from ATom (number of observations: 1003), NOAA weekly surface flask network (number of observations: 781), in situ network (only selected 1 – 2 samples per day; number of observations: 2559), and biweekly – monthly aircraft profiling sites (only data above 1 km above ground were selected at North American sites; number of observations: 4824).

1070  
1071  
1072  
1073  
1074  
1075  
1076  
1077  
1078  
1079

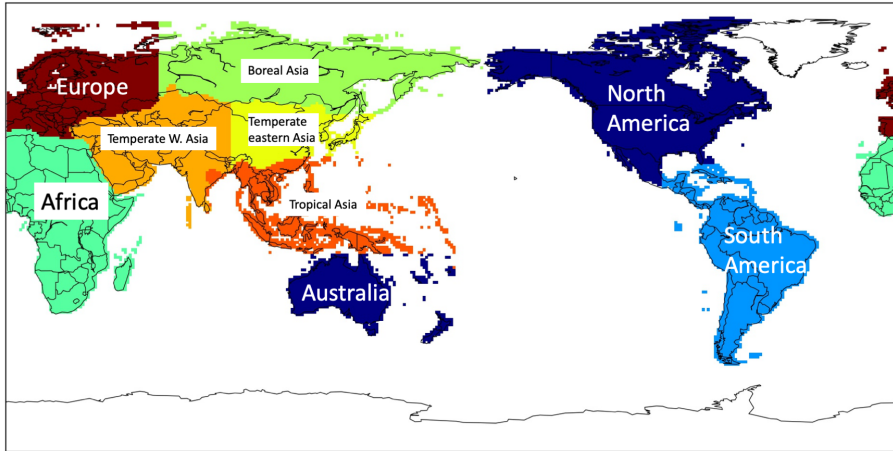






1083  
1084  
1085  
1086  
1087  
1088  
1089  
1090  
1091  
1092  
1093

**Fig. 2.** Prior CFC-11 emissions used in this study. Priors of “population\_67” and “population\_40” have global CFC-11 emissions of 67 Gg yr<sup>-1</sup> and 40 Gg yr<sup>-1</sup>. Compared to the prior “population\_67”, priors of “population\_87\_NA”, “population\_87\_SA”, “population\_87\_Af”, “population\_87\_Eu”, “population\_87\_Au”, “population\_87\_BA”, “population\_87\_TEA”, “population\_87\_TWA”, and “population\_87\_TA” have a global emission total of 87 Gg yr<sup>-1</sup> with additional 20 Gg yr<sup>-1</sup> emissions imposed over North America, South America, Africa, Europe, Australia, boreal Asia, temperate eastern Asia, temperate western Asia, and tropical Asia, respectively.



1094  
1095 **Fig. 3.** Emissive regions defined for this analysis: North America, South America, Europe, Africa,  
1096 Australia, and Asia; Asia was further divided into Boreal Asia, Temperate Eastern Asia, Temperate  
1097 Western Asia, and Tropical Asia.  
1098  
1099  
1100  
1101  
1102  
1103  
1104  
1105

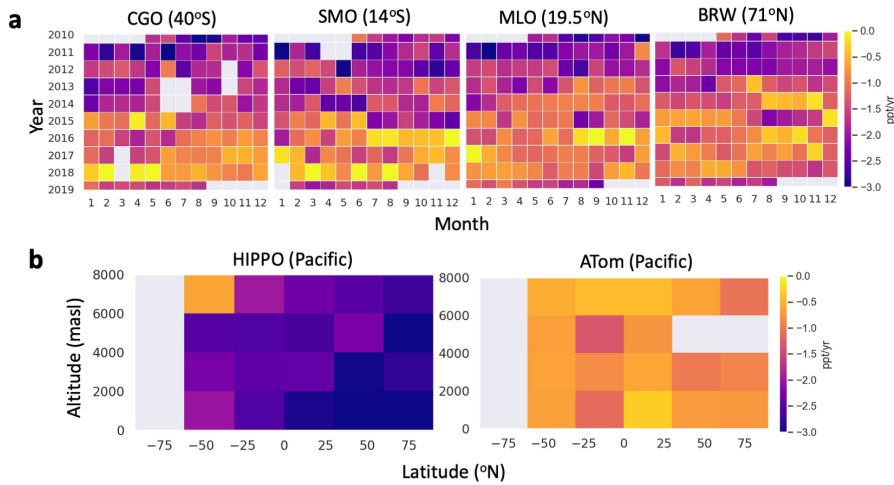
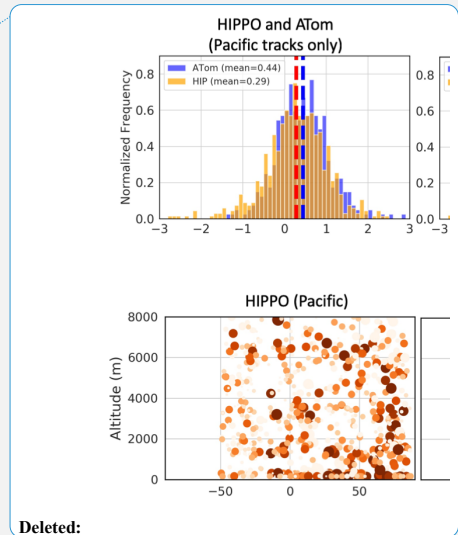


**Fig. 4.** Annual growth rates of atmospheric CFC-11 measured at four surface flask sampling sites over the Pacific Ocean basin from 2010 – 2019 (a) and CFC-11 growth rates measured during the selected HIPPO and ATom aircraft profiling surveys that took place during Nov 2009 - Sep 2011 and Aug 2016 - May 2018, respectively (b). Each grid cell indicates an annual difference relative to the prior year for that given month (in panel a) or location (in panel b). Gray cells indicate periods or locations with no data. The four surface sites plotted in panel (a) are Cape Grim, Tasmania, Australia (CGO), Tutuila, American Samoa (SMO), Mauna Loa, Hawaii, United States (MLO), and Pt. Barrow, Alaska, United States (BRW).

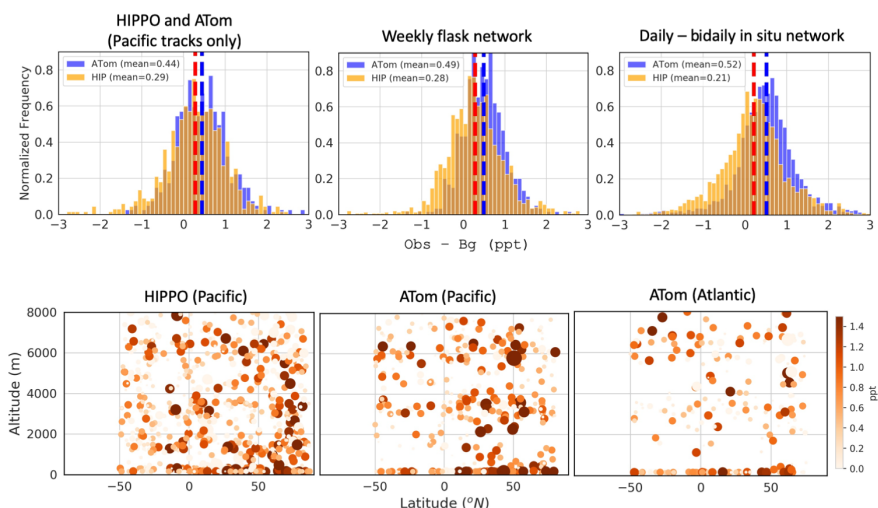
Deleted: by

Deleted: with no data.

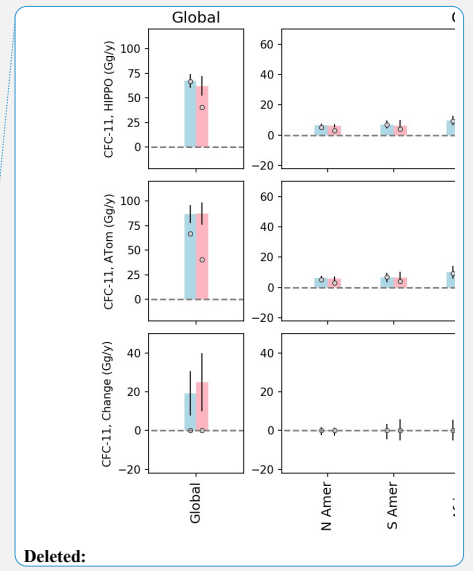
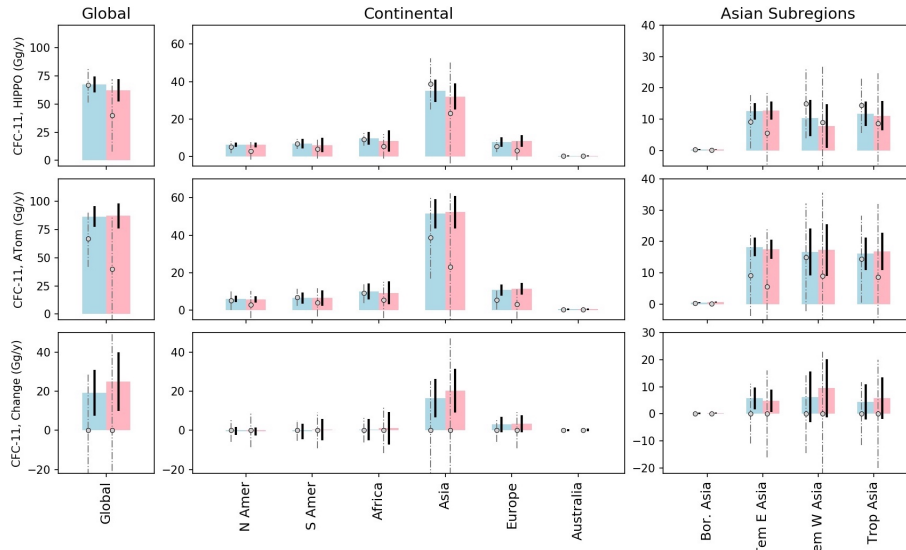


Deleted:

1106  
1107  
1108  
1109  
1110  
1111  
1112  
1113  
1114  
1115  
1116  
1117



1121  
 1122 **Fig. 5.** Enhancements of CFC-11 mole fractions relative to background air mole fractions,  
 1123 measured by three independent networks during Nov 2009 – Sep 2011 (HIPPO period) and Aug  
 1124 2016 – May 2018 (ATom period). (a) Histograms of enhancements of CFC-11 mole fractions  
 1125 measured from flasks collected over the Pacific Ocean basin during the HIPPO and ATom  
 1126 campaigns (left panel), in flasks collected in the NOAA weekly surface sampling network during  
 1127 those periods (middle panel), and measured from the NOAA in situ sampling network in both  
 1128 periods (right panel). Orange bars indicate normalized frequencies of enhancements observed in  
 1129 the HIPPO period, whereas blue bars indicate normalized frequencies of enhancements observed  
 1130 in the ATom period. Red and blue dashed lines denote the mean mole fractions observed during  
 1131 HIPPO and ATom periods. (b) Atmospheric CFC-11 mole fraction enhancements measured from  
 1132 flasks above the Pacific Ocean Basin during HIPPO (left) and ATom (middle), and above the  
 1133 Atlantic Ocean Basin during ATom (right). Both color shading and size of the symbols are  
 1134 proportional to the magnitude of mole fraction enhancements.  
 1135

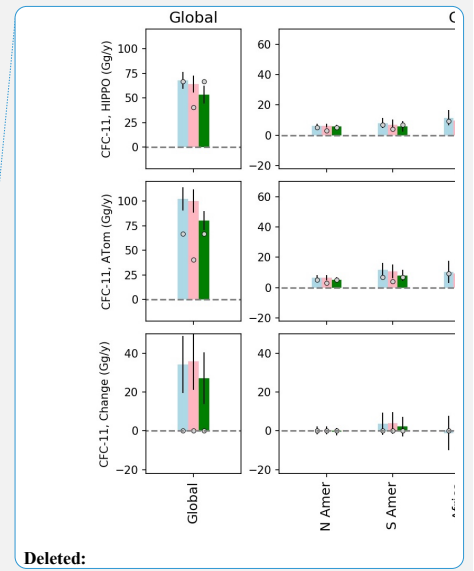
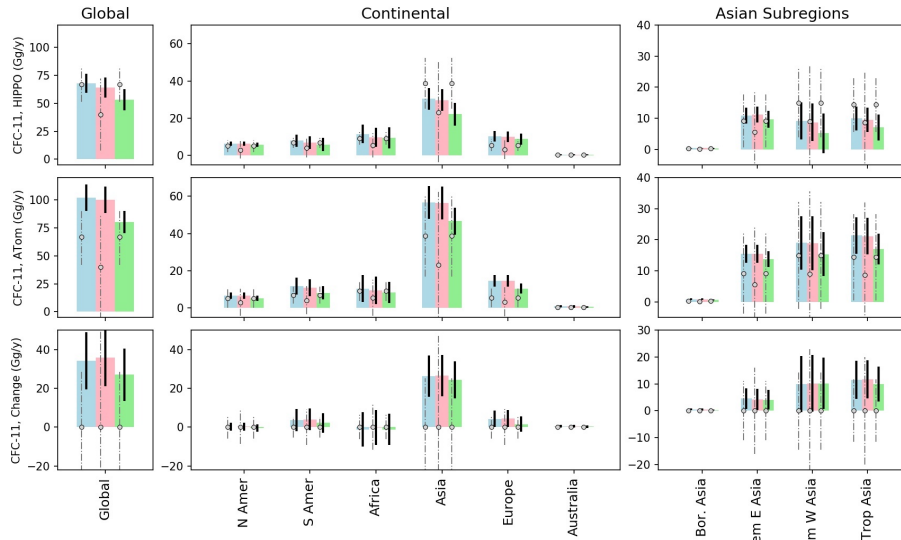


1136  
1137  
1138  
1139  
1140  
1141  
1142  
1143  
1144  
1145  
1146  
1147  
1148

**Fig. 6.** Prior (circles) and posterior (bars) CFC-11 emissions derived for the globe, continents, and Asian subregions, from the “flask-only” inversions for the HIPPO period (upper three panels), the ATom period (middle three panels), and emission differences between the two periods (lower three panels). In each region and from the left to right, open circles denote the two assumed prior emissions (“population 67” and “population 40”) with zero changes between the HIPPO and ATom periods. Gray dashed lines indicate  $2\sigma$  prior uncertainties. Light blue and pink bars correspond to posterior emissions derived from the two different priors. Black errorbars of CFC-11 emissions derived for the HIPPO and ATom periods (the upper and middle panels) indicate  $2\sigma$  posterior uncertainties derived from individual inversions. Errorbars for the derived CFC-11 emission changes (the lower panels) between the HIPPO and ATom periods were calculated from the square root of the sum squared errors shown in the upper and middle panels.

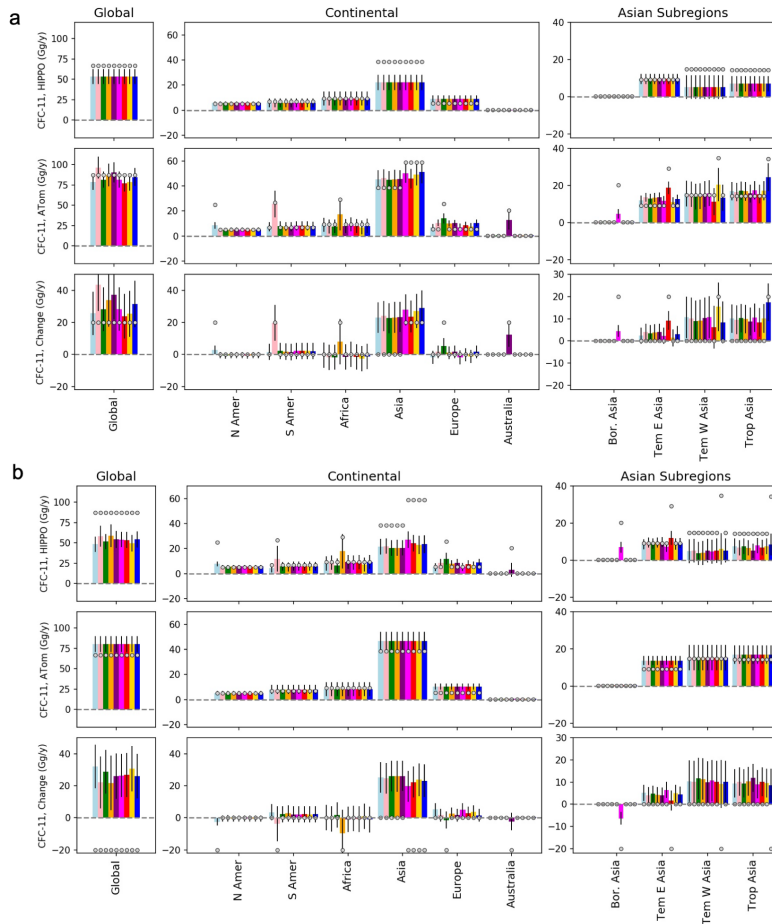
Deleted: ), considering  
 Deleted: emission  
 Deleted: in the prior assumptions. Open circles denote the assumed prior emissions.  
 Deleted: indicate  
 Deleted: with  
 Deleted: (population\_67 and population 40 shown in Fig. 2). Errorbars  
 Deleted: based  
 Deleted: of  $2\sigma$   
 Deleted: derived for  
 Deleted: HIPPO  
 Deleted: ATom inversions





1163  
 1164 **Fig. 7.** Prior (circles) and posterior (bars) CFC-11 emissions derived for the globe, continents, and  
 1165 Asian subregions, from the “flask + in situ” inversions for the HIPPO period (upper three panels),  
 1166 the ATom period (middle three panels), and emission differences between the two periods (lower  
 1167 three panels). In each region and from the left to right, open circles denote the three assumed prior  
 1168 emissions (“population 67”, “population 40”, and “population 67”) with zero changes between  
 1169 the HIPPO and ATom periods. Light blue, pink, and green bars indicate posterior emissions  
 1170 derived from the three priors and two different backgrounds, as described in inversions JD = 3 - 5  
 1171 in Table S1.  
 1172

Deleted:  
 Deleted: ”  
 Deleted: ), considering  
 Deleted: emission  
 Deleted: in the prior assumptions.  
 Deleted: dark  
 Deleted: different  
 Deleted: background in  
 Deleted: ensembles #  
 Deleted: #  
 Deleted: described  
 Deleted: Errorbars of CFC-11 emissions derived for the HIPPO and ATom periods (the upper and middle panels) indicate  $2\sigma$  uncertainties derived from individual inversions. Errorbars for the derived CFC-11 emission changes between the HIPPO and ATom periods were calculated based the sum of  $2\sigma$  errors derived for the HIPPO and ATom inversions.



1190  
 1191 **Fig. 8.** Testing the sensitivity of assumed prior emission changes on the inversion-derived emission  
 1192 changes. (a) Assume a 20 Gg yr<sup>-1</sup> emission increase between the HIPPO and ATom periods in  
 1193 individual continents and Asian subregions. (b) Assume a 20 Gg yr<sup>-1</sup> emission decrease between  
 1194 the HIPPO and ATom periods in individual continents and Asian subregions. Similar to Fig. 7,  
 1195 posterior CFC-11 emissions were derived from the “flask + in situ” inversions for the HIPPO and  
 1196 the ATom periods. In each region and from the left to right, open circles denote the prior emissions,  
 1197 as described for inversions ID = 6 - 14 in Table S1 for panel (a), and for inversions ID = 15 - 23  
 1198 in Table S1 for panel (b); different colored bars indicate the corresponding posterior emissions  
 1199 derived from inversions ID = 6 - 14 (a) and ID = 15 - 23 (b) as described in Table S1.

- Deleted: emissions and
- Deleted: ”
- Deleted: period
- Deleted: period. Open
- Deleted: . Different color bars indicate posterior emissions derived from inversions ensembles #6 - #14
- Deleted: from
- Deleted: ensembles #
- Deleted: #
- Deleted: described
- Deleted: ). Errorbars of CFC-11 emissions derived for the HIPPO and ATom periods indicate 2σ uncertainties derived from individual inversions. Errorbars for
- Deleted: derived CFC-11 emission changes between the HIPPO
- Deleted: ATom periods were calculated based the sum of 2σ errors derived for the HIPPO and ATom inversions.

**Page 5: [1] Deleted** **Lei Hu** **1/7/22 11:55:00 AM**

▼

**Page 5: [2] Deleted** **Lei Hu** **1/7/22 11:55:00 AM**

▼

**Page 5: [3] Deleted** **Lei Hu** **1/7/22 11:55:00 AM**

▼

**Page 5: [4] Deleted** **Lei Hu** **1/7/22 11:55:00 AM**

▼

**Page 5: [5] Deleted** **Lei Hu** **1/7/22 11:55:00 AM**

▼

**Page 5: [6] Deleted** **Lei Hu** **1/7/22 11:55:00 AM**

▼